

MARTINI Coarse-grained Force Field for Thermoplastic Starch Nanocomposites

Ankit Patidar and Gaurav Goel*

Department of Chemical Engineering, Indian Institute of Technology Delhi, New Delhi, India

E-mail: goelg@chemical.iitd.ac.in

Abstract

Thermoplastic starch (TPS) is an excellent film-forming material, and the addition of fillers such as tetramethylammonium-montmorillonite (TMA-MMT) clay has significantly expanded its use in packaging applications. We first used all-atom (AA) simulation to predict several macroscopic (Young's modulus, glass transition temperature, density) and microscopic (conformation along 1–4 and 1–6 glycosidic linkages, composite morphology) properties of TPS melt and TPS–TMA-MMT composite. The interplay of polymer-surface (weakly repulsive), plasticizer-surface (attractive), and polymer-plasticizer (weakly attractive) interactions lead to conformational and dynamics properties distinct from those in systems with either attractive or repulsive polymer-surface interactions. A subset of AA properties was used to parameterize the MAR-

TINI coarse-grained (CG) force field (FF) for the melt and composite systems. Specifically, we determined the missing bonded parameters of amylose and amylopectin and rationalized the bead types for 1–4 and 1–6 linked α -D glucose using two-body excess entropy, density, and bond and angle distributions in AA TPS melt. The MARTINI CG model for TPS was combined with an existing parameter set for TMA-MMT. The liquid-liquid partitioning-based MARTINI-2 FF shows freezing and compaction of polymer chains near the sheet surface, further accentuated by lowering of dispersive interactions between pairs of high covalent-coordination ring units of TPS polymers and MMT sheet. A rescaling of the effective dispersive component of TPS-MMT cross-interactions was used to optimize the FF for the composite system, with structural (chain size distribution), thermodynamic (chain conformational entropy, density), and dynamic (self-diffusion

coefficient) properties obtained from long AA simulations forming the constraints for optimization. The obtained CG FF parameters provided excellent estimates for several other properties of the melt and composite systems not used in parameter estimation, thus establishing the robustness of the developed model.

1 Introduction

Thermoplastic starch (TPS) is obtained by gelatinization of native starch, a polysaccharide consisting of amylose and amylopectin, by addition of plasticizers, such as glycerol, sorbitol, water, etc.¹ Amylose is a linear polymer of 1-4 linked α -D glucose and amylopectin has additional 1-6 branching on the 1-4 backbone (Figure S4). Low cost, excellent film-forming properties (low glass transition temperature, easy melt processability, acceptable elongation at break),^{2,3} low oxygen permeability, and biodegradability⁴ make TPS an attractive option for food packaging, drug delivery, paper additive, etc.⁵⁻⁹ However, its poor mechanical properties (low Young's modulus and tensile strength, limited elongation at break)¹⁰⁻¹² and low moisture resistance¹³ necessitate the addition of components with complementary properties, such as addition of nanofillers,¹⁴⁻¹⁶ blending with other polymers.^{17,18} Several stud-

ies have shown improvement in tensile strength and moisture barrier of TPS films on adding surface polarity-matched phyllosilicate clays, such as organically-modified montmorillonite (MMT).^{10,15,19-23} In general, wide availability, low cost, and surface tunability make MMT a particularly suitable nanofiller for modulating properties of polymeric materials.^{14,24,25} For example, blending with polylactic acid (PLA) was shown to nominally reduced water sorption of a TPS film, but microphase separation of two polymer phases led to poorer mechanical properties.²⁶ Here, addition of 1% Na-MMT) resulted in a lower number-average domain diameter of PLA (from 21.3 μm to 13.45 μm) and an improved tensile strength (from 5.63 MPa to 7.95 MPa). The properties of composite materials depend on various factors, including polymer chemistry, polymer-filler interactions, and filler aspect ratio, which consequently determine filler particle dispersion and composite's morphology.^{14,16,23,27} The identification of specific nanoparticles and other topological parameters for improving properties of interest and optimization in the composition-property space requires a time- and resource-intensive exploration,^{14,16,23,27} made more challenging for starch-based composites due to a large diversity in the base components (TPS is a multi-component material) and chemical heterogene-

ity present in each component (e.g., primary structure diversity of amylopectin). Molecular dynamics (MD) simulations provide a viable first step to characterize structure-property relationships of multi-component systems and obtain narrow bounds on the composition space for a target property, thus complementing efforts to develop new polymer composites.²⁸⁻³¹ MD simulations using all-atom (AA) representation of polysaccharides³²⁻³⁶ have been shown to accurately predict a variety of properties of some simple systems, for example, glass transition temperature and Young's modulus of TPS melt,^{37,38} chain size distribution of amylose in water,³⁹ and crystalline packing of cellulose fibers.⁴⁰ However, slow relaxation dynamics and disparate length scales of the components preclude the applicability of AA simulations to several systems of fundamental and technological interest. For example, the characteristic relaxation time of a small 20-unit amylose ($3260.86 \text{ g mol}^{-1}$) in its melt was reported to be 404.7 ns at 700 K (much above typical processing temperature),⁴¹ eight orders of magnitude higher than the AA time step even for this limiting case. The presence of high molecular weight polymer chains (radius of gyration $\sim 50 \text{ nm}$) and highly anisotropic fillers such as $\sim 200 \text{ nm}$ diameter bentonite clay) bentonite clay in TPS film make property determination using AA

simulations computationally intractable. The coarse-grained (CG) force fields, wherein some of the AA degrees of freedom are integrated out, can be ~ 100 -fold faster than AA simulations even at the lower-end of coarse-graining. CG approaches employed to study polymer composites at some level of relevant length- and timescales can be broadly divided into two categories based on the treatment of interaction between various components. In one case, the enthalpic contribution is modeled by a minimal, single-parameter effective interaction between large units (a Kuhn monomer of $\sim 1 \text{ nm}$, a nanoparticle, etc.). The effective interaction parameters are then used in mesoscale dissipative particle dynamics (DPD) simulations⁴²⁻⁵⁰ or field-based / integral-equation theories,⁵¹⁻⁶³ to characterize structure and thermodynamics of diverse polymeric systems. In a multiscale DPD scheme, integral equation theory was used to obtain an effective softcore interaction between polymer chains, enabling use of a very large time step (ps - ns),^{64,65} and its application to polyethylene melt^{66,67} and blends⁶⁸ showed a fairly good comparison with structural (radius of gyration and radial distribution function) and dynamic properties (diffusion coefficient of chain center of mass) obtained in united atom (UA) simulations. These methods, based on a simplified model for enthalpy, have provided

qualitative and, in several cases, quantitatively accurate predictions for the phase diagram and the equilibrium properties of large-scale polymer systems.^{49,69–72} The interaction parameter is dependent on the thermodynamic state variables (temperature, pressure, composition) and needs to be obtained semi-empirically from molecular simulations, liquid-state theories, or experiments at a sufficiently large number of state points, wherein an increase in system heterogeneity significantly expands the phase space for interaction parameter determination.

Chemical-specific CG models provide an alternative with possible state-point transferability and good accuracy across highly diverse systems. Herein, 4-10 atoms are grouped in a single bead, with effective pair interaction obtained from a combination of AA simulations and experimental data. This mapping from AA to CG can be obtained by using structure distribution functions as constraints, as done in iterative Boltzmann inversion (IBI)^{73,74} and force matching⁷⁵ or by using thermodynamic properties as constraints, such as equilibrium partitioning between polar and apolar solvents used for MARTINI CG force field.⁷⁶ In structure-based methods, parameters need to be optimized using data from multiple state points,⁷⁷ and can still ex-

hibit environmental dependence. The MARTINI force field has been demonstrated to mitigate these limitations. For instance, the MARTINI CG parameters for polypropylene were shown to accurately reproduce (values obtained in AA simulation) the radius of gyration in various chemical environments (good, bad, and theta solvent conditions) as well as the partitioning of polyethylene-polypropylene blends near phospholipid membranes.⁷⁸ However, a reduction in self- (saccharides molecules)^{79,80} or cross-interaction (graphene-small organic molecules)^{81–83} was required in some cases, highlighting a need for further parameter optimization.

Given the wide interest in phyllosilicate-based composites, we have developed MARTINI CG parameters for a TPS-[tetra methyl ammonium(TMA)]-MMT system in this study. The CG parameters for some individual TPS components (amylose,⁸⁴ sorbitol,⁸⁵ water⁸⁶) and TMA-MMT⁸⁷ have been shown to reproduce several properties determined from AA simulations. However, to the best of our knowledge, MARTINI CG FF for a TPS melt or its composites is not available. Here, we have reparameterized and developed missing bonded parameters for the CG model of two polymeric components (amylose and amylopectin) by using data from AA simulation of TPS melt, ra-

tionalized the bead type assignment for 1-4 and 1-6 linked α -D glucose, and determined the cross-interaction levels for all TPS and TMA-MMT beads. The developed parameter set was extensively validated by comparing structural (chain size distribution), thermodynamic (chain conformational entropy, density, excess entropy), and dynamic (self-diffusion coefficient) properties against sufficiently long AA simulations. Finally, predictions for radial distribution function (RDF) and two-body excess entropy in the composite system, two properties not used in CG parameterization, were used to test the robustness of developed CG parameters.

2 Methods

2.1 System and Simulation Details

2.1.1 AA MD Simulations

The initial structures and CHARMM36^{88,89} parameters of amylopectin (thirty-six monomers), amylose (eighteen monomers), and sorbitol were obtained using CHARMM-GUI.⁸⁸⁻⁹⁰ We used a TIP3P water model and the INTERFACE force field⁹¹ for the TMA-MMT sheet. A low density ($\rho = 117.62 \text{ kg m}^{-3}$) TPS configuration (55327 atoms) consisting of (weight

percent) 50 % amylopectin, 20 % amylose, 29 % sorbitol, and 1 % water was prepared in Packmol.⁹² A high-density system was obtained by rescaling the box in multiple steps followed by temperature-pressure (T - P) annealing cycles (details in Section 5.1). Densities of 1227.75 and 1227.62 kg m^{-3} at 613 K, 1 bar were obtained after the first two T - P cycles, respectively, indicating the adequacy of only one cycle. The obtained value compares well with a TPS melt density of 1369.80 kg m^{-3} from AA simulation at 550 K, 1 bar³⁷ and 1442 kg m^{-3} at 300 K, 1 bar from experiments.⁹³ For composite simulations, a 10.32 nm \times 10.71 nm \times 1.2 nm TMA-MMT sheet, connected across x - y periodic boundaries to model an infinitely large sheet, was placed between two equilibrated TPS melt boxes (Figure S11 (a)). An 82.5 % TPS and 17.5 % TMA-MMT system with dimensions 10.32 nm \times 10.71 nm \times 11.40 nm was obtained after one T - P annealing cycle. All melt and composite properties were calculated from a 1100 ns MD simulation started from the configuration at the end of the first T - P annealing cycle. MD simulations were performed using GROMACS 2021.4,⁹⁴ with a time step of 1 fs, V-rescale thermostat ($\tau=1$ ps),⁹⁵ and either the Berendsen barostat ($\tau=2$ ps, first 100 ns)⁹⁶ or the Parrinello-Rahman barostat ($\tau=5$ ps).⁹⁷

2.1.2 CG MD Simulations

The initial CG structures for TPS melt and TPS–TMA–MMT composite were obtained from the last frame of the corresponding 1100 ns AA simulation by placing CG beads at the center of mass positions (Equation S3) of constituent atoms (mapping scheme in Figure 1). Force field parameters at the level of MARTINI v2.2⁷⁶ were either directly used, if available and found suitable, or were obtained using reference AA simulations. For all CG simulations, a time step of 5 fs was used, the system was coupled to the V-rescale thermostat ($\tau=1$ ps) and either the Berendsen barostat ($\tau=8$ ps, first 100 ns) or the Parrinello-Rahman barostat ($\tau=12$ ps). The CG potential is given as per Equation 1.

$$U = 4\epsilon_{ij} \left[\left(\frac{\sigma_{ij}}{r_{ij}} \right)^{12} - \left(\frac{\sigma_{ij}}{r_{ij}} \right)^6 \right] + \frac{q_i q_j}{4\pi\epsilon_0\epsilon_{rel}r_{ij}} + \frac{1}{2}K_l(l_{ij} - l_0)^2 + \frac{1}{2}K_\theta(\cos\theta_{ijk} - \cos\theta_0)^2 + K_\phi[1 + (\cos\phi_{ijkl} - \cos\phi_0)], \quad (1)$$

where σ_{ij} , ϵ_{ij} , q , and ϵ_{rel} are bead diameter, interaction strength, bead charge, and relative dielectric constant, respectively. The force constants for bond (l_{ij}), angle (θ_{ijk}), and torsion (ϕ_{ijkl}) potentials are K_l , K_θ , and K_ϕ , respectively. $\sigma_{ij} = 0.47$ nm for the regular beads (four heavy atoms) and 0.43 nm for the small

beads (s-type, 2-3 heavy atoms). The choice of ϵ_{ij} is linked to the functional group(s) in the CG bead, with primary categorization defined as polar (P), neutral (N), apolar (C), or charged (Q), and level within a category assigned by an integer in range 0–6 (e.g., P4 is more polar than P1, C4 is more apolar than C1). We used a P4c bead for three diol units of sorbitol (see Figure 1), a CG model shown to be in qualitative agreement with experiments on the kinetics of aggregation of amyloid- and elastin-like peptides in presence of sorbitol.⁸⁵ The refined polarizable model was used for water since the standard MARTINI water model (one P4 bead) exhibits unphysical freezing near surfaces.^{86,98} The parameters for the TMA–MMT sheet were taken from Khan and Goel⁸⁷ who found several properties of hydrophobic polymers–TMA–MMT composites to be in a good agreement with AA simulations (Supplementary Information Figure S10). The bonded parameters for 1–4 linked α -D glucose were either taken from Lopez et al.’s study⁸⁴ on short amylose chains in polar (water) and non-polar (nonane) solvents (labeled CG1 model) or obtained as best-fit models to the corresponding pair, triplet, and quadruplet distributions in AA simulations of TPS melt (labeled CG2 model). The bonded parameters for 1-6 linked α -D glucose were similarly obtained from the AA simulations of TPS

melt (for both CG1 and CG2).

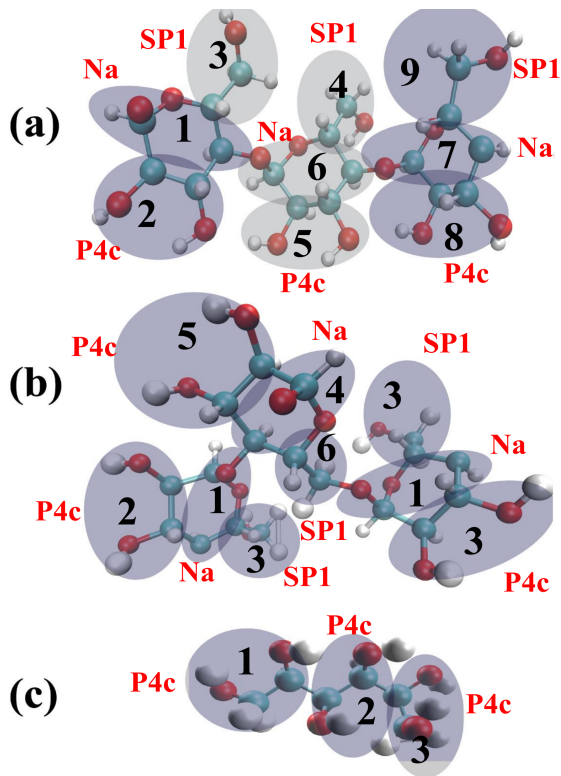


Figure 1: Mapping scheme for TPS components. (a) A trimeric 1-4 bonded α -D glucose oligomer (represents terminal and middle monomer of amylose), (b) A trimeric 1-4 or 1-6 bonded α -D glucose oligomer (represents the branch point in amylopectin), and (c) sorbitol. Red, white, and cyan represent oxygen, hydrogen, and carbon atoms, respectively, with atoms in a single CG bead grouped within shaded circles. The bead number and type are indicated by black and red color labels, respectively.

2.2 Property Calculation

In the composite system, the near- and far-sheet regions were classified based on density profiles of TPS components along the normal to the TMA-MMT sheet (z -axis). For polymer chains, the z -component of the distance of the center of mass (COM) of a given trimeric seg-

ment (\sim persistence length (0.86 nm) of amylose) from the sheet was used to classify it as a near or a far segment, with a chain labeled as a near/far-region chain if $> 70\%$ segments were in the near/far region. Unless otherwise indicated, all properties are calculated at 613 K and 1 bar using the last 900 ns trajectory (a 200 ns convergence time for some properties in total 1100 ns trajectory).

2.2.1 Structural and Dynamic Properties

Density, radial distribution function (RDF), persistence length (l_p), and radius of gyration (R_g) of TPS melt and composite systems were estimated using GROMACS utilities. COMs of atoms making the CG beads were used for RDF calculation in the AA simulations to allow comparison with the CG simulations. An exclusion of up to four CG-bonded neighbors or up to 16 AA-bonded neighbors, equivalent to an average COM separation of 1.29 nm, was used for RDF calculation. For the composite system, a 2D RDF was calculated in 0.37 nm slices parallel (in the $x - y$ plane) to the TMA-MMT sheet. The data is reported as average over four slices in the near region and five slices in the far region.

The diffusion coefficients of sorbitol and trimeric polymer chain segments (amylose and

amylopectin) were calculated from the corresponding temporal profile of mean-square-displacement ($MSD(t)$) using the Einstein’s diffusion equation (Equation S2). The AA and CG data were compared using the normalized diffusion coefficient, D_n , defined as the ratio of lateral diffusion coefficient in the composite (in the $x-y$ plane) to the melt diffusion coefficient.

2.2.2 Thermodynamic Properties

The TPS melt was cooled from 613 K to 150 K in steps of 25 K, wherein a 4 ns NPT simulation was performed at each step, with last 500 ps trajectory at each step used for density calculation. The intersection of linear fits to the temperature-density data in the rubbery (high temperature) and glassy (low temperature) regions was used as an estimate for $T_{g,sim}$. The Williams-Landel-Ferry (WLF) equation⁹⁹ (Equation 2) was used to obtain an estimate for the glass transition temperature at a typical experimental cooling rate of 10 K min^{-1} ($T_{g,exp}$) from the simulation estimate $T_{g,sim}$ obtained at $3.75 \times 10^{11} \text{ K min}^{-1}$.

$$\log_{10} \frac{\tau_{g,sim}}{\tau_{g,exp}} = \frac{-C_1 * (T_{g,sim} - T_{g,exp})}{C_2 + T_{g,sim} - T_{g,exp}}, \quad (2)$$

where $C_1 = 17.44$ and $C_2 = 51.6 \text{ K}$ (constant for several polymers), $\tau_{g,sim}$ and $\tau_{g,exp}$ are the

inverse of cooling rates in simulation and experiment, respectively.

The pairwise ($S_{2,\alpha\beta}$) and total (S_2) two-body excess entropy was calculated using the corresponding $RDFs$ ($g_{\alpha\beta}$) as per Equations 3 and 4 (integral calculated up to 2.5 nm), respectively.¹⁰⁰

$$S_{2,\alpha\beta} = -2\pi\rho \int_0^\infty g_{\alpha\beta}(r) \ln g_{\alpha\beta}(r) - [g_{\alpha\beta}(r) - 1] r^2 dr \quad (3)$$

$$S_2 = \sum_{\alpha,\beta} x_\alpha x_\beta S_{\alpha\beta}, \quad (4)$$

where x_α and x_β are the mole fractions of α and β components, respectively. Equation 3 was suitably modified to integrate 2D RDFs for the composite system over cylindrical disks (Equation S1).

The configurational entropy (S_c) of amylose and amylopectin chains was calculated from the covariance matrix of each chain (after removing rigid-body translational and rotational motion) using the Schlitter’s equation,¹⁰¹ implemented with GROMACS utility `anaeig`.

2.2.3 Mechanical properties

Young’s modulus of TPS melt and TMA-MMT sheet was calculated from AA simulations at 300 K and 1 bar. A uniaxial strain along x -axis

was added in steps of 0.1% of the initial box length, with a 2 ns *NPT* simulation at each step (anisotropic pressure coupling for y and z). The stress at every step was calculated from the P_{xx} Virial component averaged over the last 300 ps of the trajectory, and the slope of the stress-strain curve in the linear regime was used to estimate the Young’s modulus. Maximum strain value (σ_{\max}) marks the onset of the plateau region in the stress-strain profile.

3 Results and discussion

3.1 Validation of TPS AA parameters

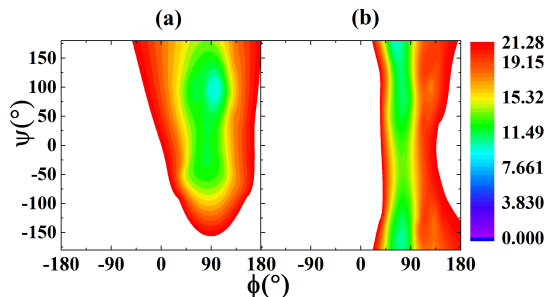


Figure 2: Polymer chain conformation at inter-ring links in a TPS melt. ϕ - ψ torsion angle distribution in TPS melt for **(a)** 1-4 and **(b)** 1-6 glycosidic linkages, shown as the potential of mean force (PMF) profile (color scale in kJ mol^{-1}) obtained from the probability distributions averaged over 900 ns AA simulation at 613 K and 1 bar.

The local chain conformation in TPS melt was characterized using the torsion angles for 1-4 and 1-6 glycosidic linkages, viz. $\phi = \angle O_5 - C_4 - O_1 - C_1$

and $\psi = \angle C_1 - O_1 - C_4 - C_3$ for 1-4, and $\phi = \angle O_5 - C_1 - O_1 - C_6$ and $\psi = \angle C_1 - O_1 - C_6 - C_5$ for 1-6 (Figure S5). Figure 2 (a) shows syn- and anti-states as two dominant conformers for the 1-4 linkage, with peak at (ϕ, ψ) equal to $(90^\circ, 100^\circ)$ and $(100^\circ, -50^\circ)$, respectively. This agrees well with the AA simulations of an amylose oligomer in water using the same force field (*syn*: $(90^\circ, 100^\circ)$ and *anti*: $(80^\circ, -50^\circ)$)³⁹ and XRD spectroscopy of a hydrated cycloamylose (*syn*: $(103.6^\circ, 115.1^\circ)$ and *anti*: $(88.1^\circ, -48.4^\circ)$).¹⁰² The conformational space of 1-6 linkage has a single peak at $(70^\circ, 180^\circ)$ (Figure 2(b)), in close agreement with replica exchange simulation and NMR spectroscopy on α -1-6 glucopyranoside dimer $((\phi, \psi) = (70^\circ, 180^\circ))$.¹⁰³

A TPS melt density of 1.43 g cm^{-3} at 300 K compares well with a value of 1.47 g cm^{-3} obtained from both experimental measurements and simulations for a 70:30 (*wt%*) amylopectin-sorbitol blend at 300 K.^{37,38} The available experimental data on the glass transition temperature (T_g) and Young’s modulus (E_i), both directly linked to the nature of intermolecular interactions and atomic-scale packing, allow an additional test for force field parameters and simulation convergence. We obtained $T_g = 405 \text{ K}$ from temperature-density variation

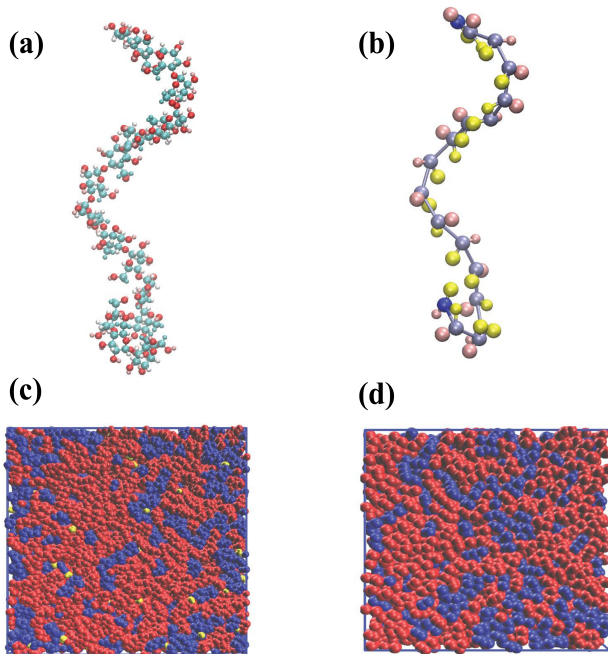


Figure 3: AA and CG representation of TPS melt. A 18-mer amylose chain in **(a)** AA (oxygen, hydrogen, and carbon atoms in red, white, and cyan, respectively) and **(b)** CG (P1, SP1, P4c, and Na beads in blue, pink, yellow, and ice blue, respectively) representations. **(c)** and **(d)** TPS melt simulation box obtained at end of 1100 ns AA simulation at 613 K and 1 bar in AA and CG, respectively. Polymer, sorbitol, and water beads in red, blue, and yellow, respectively.

obtained at a cooling rate of $3.75 \times 10^{11} \text{ K min}^{-1}$ in AA simulation of TPS melt (Figure S3), which yields a $T_g = 325 \text{ K}$ on scaling to the experimental cooling rate of 10 K min^{-1} using the WLF equation (Equation 2). This is in excellent agreement with a value of 321 K obtained in a simulation of 70:30 amylopectin-sorbitol blend³⁸ and experimental estimates in range 300 K – 340 K for barley starch with 29% glycerol (a small molecule plasticizer like sorbitol).¹⁰⁴ $E_{\text{TPS}} = 5.2 \text{ GPa}$ and $\sigma_{\text{max}} = 270 \text{ MPa}$ obtained from the stress-strain variation for TPS melt at 300 K (Figure S2) compare well

Table 1: A comparison of various properties of TPS melt obtained from AA simulations with previous simulations and experimental measurements.

Property	Present Simulations	Previous Experiments	Previous simulations
1–4 ψ°	$100^\circ, 50^{\circ 1}$	$115.1, 48.4^{\circ 2}$	$90^\circ, 50^{\circ 3}$
1–4 ϕ°	$90^\circ, 100^{\circ 1}$	$103.6^\circ, 88.1^{\circ 2}$	$90^\circ, 80^{\circ 3}$
1–6 ψ°	$90^\circ, 180^{\circ 1}$	$89.8^\circ, 180^{\circ 4}$	-
1–6 ϕ°	$70^{\circ 1}$	$70^{\circ 4}$	-
$\rho, \text{g cm}^{-3}$	1.43^5	1.47^6	1.47^6
T_g, K	325^7	$300\text{--}340^8$	321^6
$E_{\text{TPS}}, \text{GPa}$	5.2^9	1.25^6	4.3^6
$E_{\text{MMT}}, \text{GPa}$	171.95^9		171^{10}

¹The ϕ, ψ torsion angle distribution from the AA simulation of TPS melt at 613 K and 1 bar

²XRD spectroscopy of hydrated cycloamylose¹⁰²

³AA simulation of 9-mer Amylose in water³⁹

⁴Replica exchange simulation and NMR spectroscopy on α -1–6 glucopyranoside dimer¹⁰³

⁵TPS melt density (ρ) calculated at 300 K and 1 bar

⁶70:30 (wt%) amylopectin-sorbitol melt^{37,38}

⁷Glass transition temperature (T_g) at the experimental cooling rate was obtained from the combination of temperature-density variation plot and WLF equation

⁸Native barley starch having 29% glycerol¹⁰⁴

⁹The Young’s moduli ($E_{\text{MMT}}, E_{\text{TPS}}$) was calculated from the stress-strain curve at 300 K

¹⁰Density functional theory (DFT) calculation on MMT¹⁰⁵

with $E = 4.3 \text{ GPa}$ and $\sigma_{\text{max}} = 285 \text{ MPa}$ from AA simulation of 70:30 amylopectin-sorbitol blend at 300 K , but is only within the same order of magnitude of the experimental estimate of $E = 1.25 \text{ GPa}$.³⁸ The MMT sheet modulus of 171.95 GPa from AA simulation matches the density functional theory (DFT) estimate of 178.4 GPa ¹⁰⁵ (both calculated at 300 K). Table 1 gives an itemized comparison of various properties for TPS melt calculated in this work and those reported in other studies using experimental measurements and simulations. These favorable comparisons for the local conforma-

tion of the polymer chains as well as several macroscopic properties establish the high accuracy of TPS AA parameters used in this study.

3.2 Development of CG Parameters

The developed parameter set is intended for integration with the MARTINI-2 CG forcefield as available for several polymers and nanoparticles of interest, enabling direct application to their composites with TPS. We have not used the more recent MARTINI-3 CG parameterization,¹⁰⁶ since it does not yet have a polarizable model for water.

3.2.1 CG Non-bonded Parameters for TPS melt

The three diol groups of sorbitol (Figure 1 (c)) were modeled by a P4 bead with its self-interaction lowered from level I to level II ($\epsilon=4.5\text{ kJ mol}^{-1}$), since an unphysical aggregation was observed in a low-concentration aqueous solution.⁸⁵ The refined polarizable model was used for water,^{86,98} where one neutral bead with self-interaction level V and cross-interaction level (60% to 95% of standard MARTINI water P4 bead) is connected to two virtual beads ($q=\pm 0.46$, no LJ interaction).

This was shown to provide a better representation of dielectric behaviour of water. The initial bead choice in polymer (amylose and amylopectin) was taken from an existing set of MARTINI-2 CG parameters for polysaccharides (referred to as CGLITa), obtained by parameterization on AA simulations of mono- and disaccharides in polar and apolar solvents.⁸⁴ Accordingly, hemiacetal (Figure 1(a): beads 3, 4, and 9), acetal (beads 1, 6, and 7), and diol groups (beads 2, 5, and 8) were modeled by P1, P2, and P4 beads, respectively. This is referred to as CGLITa parameter set. In this study, we used the melt density and the two-body excess entropy (higher values indicate stronger pair correlations) for polymer-polymer (given higher weight in evaluation) and polymer-sorbitol bead pairs to further optimize the bead-type assignments for amylose and amylopectin.

The CGLITa melt density of 1136 kg m^{-3} underestimates the melt density of 1214.69 kg m^{-3} in AA simulations. The S_2 (Table S1) for polymer-polymer beads is in excellent agreement with AA values (3% higher), but there is a significant deviation for the polymer-sorbitol beads (108% lower). An improved density estimate of 1253 kg m^{-3} is obtained on using s-type for all polymer beads (CGLITa-S), a recommended choice for several ring molecules.⁷⁶

All S_2 values involving a polymer bead became higher (resulting from a weakening of interaction potential), leading to a poorer estimate for polymer-polymer beads (29 % higher than AA) but an improved estimate for polymer-sorbitol beads (11 % lower than AA). A similar improvement in density, but an incorrect prediction of the crystallization behavior of a highly concentrated sugar solution was observed on replacing regular beads with small s-type beads.⁸⁴ Alternatively, on using the s-type bead only for the hemiacetal group (referred to as CGLITb), as per the bead assignment used for lipopolysaccharides,¹⁰⁷ a density of $1159.36 \text{ kg m}^{-3}$ is obtained. This represented a small improvement over CGLITa, retained almost equivalent accuracy for polymer-polymer S_2 , but polymer-sorbitol S_2 still showed a high deviation (86 % lower than AA). We made two additional changes in the bead assignments: acetal group as Na bead (recommended for obtaining accurate crystal behavior of cellulose¹⁰⁸) and one level reduction (from level I to level II) in the polymer-polymer diol bead (P4) self-interaction (shown to provide an accurate Virial coefficient and prevent unphysical aggregation of polysaccharides^{79,80}). The parameter set obtained after these two changes in CGLITb is referred to as the CG1 parameter set (Table S3). The CG1 melt density of $1141.75 \text{ kg m}^{-3}$ repre-

sented only a small improvement over CGLITa, a slightly increased polymer-polymer S_2 deviation (9 % lower than AA), and a somewhat improved polymer-sorbitol S_2 (61 % lower). Since CG1 provided the best balance in accuracy of S_2 for polymer-polymer and polymer-sorbitol pairs, we took it forward for further evaluation and optimization.

3.2.2 CG Bonded Parameters for TPS melt

The average 1–4 glycosidic bond length in AA simulation was 0.48 nm, considerably smaller than 0.56 nm in CG1, while the average 1-4-7 angle of 125° is close to the CG1 value for an amylose oligomer in an apolar solvent (120°). Accordingly, we set $l_0 = 0.48 \text{ nm}$ and $\theta_0 = 125^\circ$ for the corresponding bonded potential parameters in Equation 1. Further, the force constant (k_θ) for 1-4-5 and 1-4-6 angles needed to be doubled (w.r.t. to the CG1 value) to reproduce the AA angle distribution in TPS melt (Figure 4 (II)). This re-parameterized set, referred to as CG2 (Table S2), provided an improved representation of the three-bead angle distributions for amylose and amylopectin in TPS melt (Figure 4 (II)) and S6). The torsion distribution for the 1-4 and 1-6 linkages are well-represented by a proper dihedral potential with multiplicity 1 (Figure 4 (I)) and are taken without change

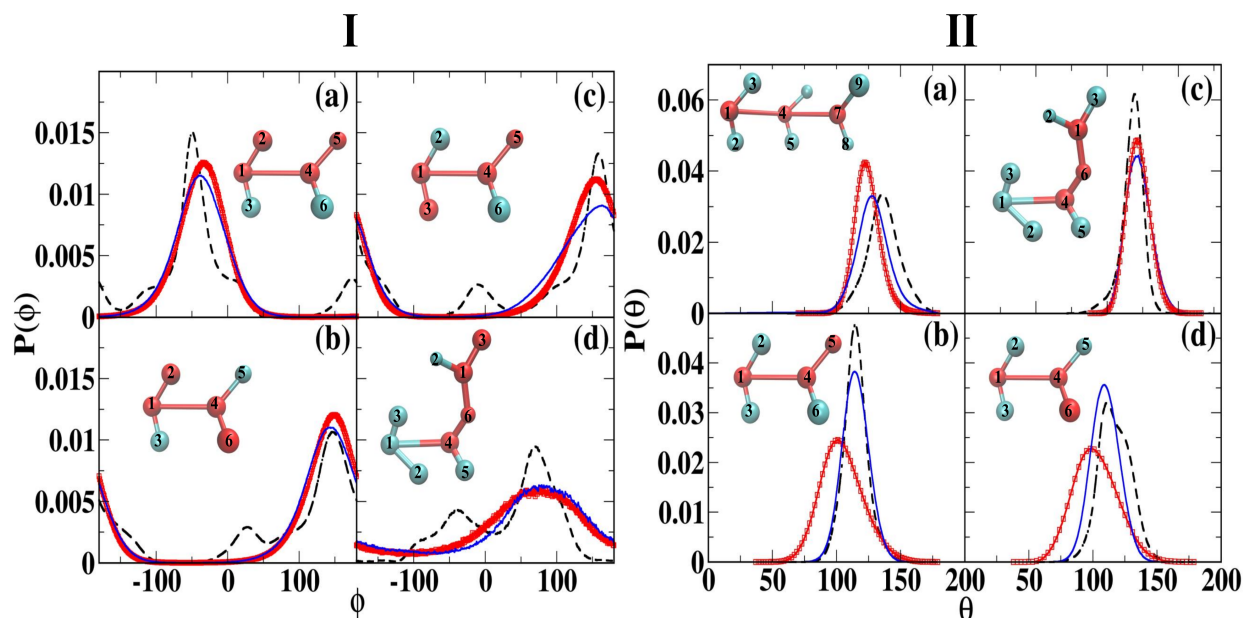


Figure 4: Bonded distribution for amylopectin AA (---), CG1 (—□—), and CG2 (—) probability distributions, $P(\phi)$ for torsions (ϕ), and $P(\theta)$ for three-bead angles (θ) were estimated from TPS melt simulations at 613 K and 1 bar. **I(a)** 2–1–4–5, **I(b)** 2–1–4–6, and **I(c)** 3–1–4–5 represent torsion distribution around the 1–4 linkage, and **I(d)** 3–1–6–4 around the 1–6 linkage. **II(a)** 1–4–7 and **II(b)** 4–6–1 represent angle distribution along 1–4 and 1–6 linkages, respectively. **II(c)** 1–4–5 and **II(d)** 1–4–6 represent intra-ring angle distributions. Bead numbers are as per Figure 1. The beads involved in the calculated quantity are shown in red and rest in cyan.

from CGLITa. Secondary peaks in the AA distribution, as seen here also, are not present in the CG distributions since the dihedral potential of multiplicity 1 is used in MARTINI FF to prevent overfitting. The CG2 parameter set also provided a slightly improved TPS melt density of $1153.74 \text{ kg m}^{-3}$ (comparable to CGLITb, better than CGLITa and CG1) and is the only set that provided a good estimate for S_2 of both polymer-polymer (2% higher) and polymer-sorbitol (22% lower). Further, amylose chain persistence length, l_p , of 0.86 nm in AA simulations compares more favorably with CG2 (0.90 nm) than CG1 (0.96 nm). For comparison, simulations of amorphous amylose

melt at 713 K gave a value of 0.9 nm with AA and 1 nm with CG MARTINI.⁴¹ The chain radius of gyration, $\langle R_g \rangle$, also follows the same trend for both amylose and amylopectin: within 5% of AA in CG2 and 15% of AA in CG1 (Table 2). The 1–4 glycosidic bond length mismatch for the CG1 model (Figure 2(II)) is the likely reason for these small but consistent differences. A lower angle stiffness and larger bond length for 1–4 bonds also lead to $\sim 10\%$ - 15% higher S_c for amylose and amylopectin chains with CG1 parameters compared to AA (Table 2). A correction for both bonded parameters in CG2 set gave S_c values within 5% of AA. Simultaneous improvements in several structural

and thermodynamic properties make the CG2 parameter set a distinct improvement over existing parameters for TPS.

3.2.3 CG Non-bonded Parameters for TPS-MMT composite

Three polymer-surface interaction dependent properties, viz. polymer normalized diffusion coefficient, D_n , radius of gyration, $\langle R_g \rangle$, and conformational entropy, S_c , were simultaneously optimized to parameterize the cross-interaction for TPS-MMT-TMA beads. A lower $\langle R_g \rangle$ and S_c near the MMT sheet in CG simulations compared to the bulk (not observed in AA) suggest a disc-like flattened configuration near the surface to maximize polymer-sheet contacts (Table 2), which also gave a much lower D_n for polymer trimeric segments and sorbitol molecules in CG simulations (Figure S9 and Table 2). This change in polymer chain conformation also affects the RDF and S_2 for all self- and cross-pairs of polymer and sorbitol beads, as discussed later in section 3.3.3. All these observations indicate that MARTINI-2 forcefield parameters overestimate solid-fluid interactions for the TPS-MMT system. A reduction in solid-fluid interaction parameter (ϵ_{ij}) was shown to be essential for accurate prediction of adsorption enthalpy of small organic molecules (butane, benzene, hexade-

cane), order-disorder transitions of hexadecane, and preferential adsorption of long-chain alkanes on graphite surfaces.⁸² Here, the effective dispersive component of ϵ_{ij} was re-scaled for all TPS-MMT pairs as per Equation 5, maintaining consistency with the parameterization strategy used for the TMA-MMT sheet.⁸⁷

$$\epsilon_{i,j} = \gamma(\epsilon_{N0,N0}) + (\epsilon_{i,j} - \epsilon_{N0,N0}), \quad (5)$$

where, i and j represent TPS and MMT beads, respectively, and γ is the scaling factor. A previous study has shown that taking the N0 bead self-interaction, $\epsilon_{N0,N0}$, as purely dispersive and scaling the dispersive component for all interaction pairs as per Equation 5 gave an accurate distribution of polar and dispersive contributions to the cleavage free energy of two TMA-MMT sheets.⁸⁷ D_n , $\langle R_g \rangle$, and S_c were calculated for the TPS-MMT system at six γ values in range 0.15-1 (Table S5 and Figure S9). The CG parameters were evaluated by using the property value in the composite normalized by the corresponding value in the melt (for the self-diffusion coefficient) or the property value in the near-sheet region normalized by the value in the far region (for the radius of gyration and the conformational entropy). This separated the effect of differences between AA and CG properties in the bulk systems (melt, far re-

Table 2: Comparison of properties determined from AA and CG simulations of TPS melt and TPS-MMT-TMA composite. The radius of gyration ($\langle R_g \rangle$), conformational entropy per CG bead (S_c), and normalized diffusion coefficient of the polymer trimeric segments (D_n) were calculated at 613 K and 1 bar, with average and standard deviation calculated from 900 ns trajectories. The green, cyan, red, and blue values indicate a relative error (in percent) of $\leq 5\%$, 5–10%, 10–15%, and $\geq 15\%$, in CG values (w.r.t. AA), respectively.

		Amylose			Amylopectin		
		near	far	melt	near	far	melt
$\langle R_g \rangle$ (nm)	AA	1.35(0.09)	1.37(0.08)	1.38(0.02)	1.74(0.15)	1.77(0.16)	1.83(0.02)
	CG1	1.49(0.18)	1.57(0.10)	1.58(0.05)	1.95(0.25)	2.01(0.19)	2.07(0.03)
	CG1red	1.53(0.13)	1.56(0.15)	1.58(0.05)	1.99(0.23)	1.99(0.23)	2.07(0.03)
	CG2	1.34(0.19)	1.45(0.12)	1.43(0.03)	1.78(0.19)	1.84(0.22)	1.83(0.06)
	CG2red	1.38(0.16)	1.40(0.16)	1.43(0.03)	1.78(0.22)	1.84(0.21)	1.83(0.06)
$\langle S_c \rangle$ (J mol ⁻¹ K)	AA	46.11(1.39)	46.73(1.64)	46.26(0.14)	45.82(2.70)	46.63(3.10)	46.23(0.11)
	CG1	44.44(4.67)	48.68(2.98)	52.16(0.11)	47.09(3.12)	51.41(3.54)	51.90(0.09)
	CG1red	48.23(1.69)	48.31(2.52)	52.16(0.11)	50.30(3.61)	51.58(2.99)	51.90(0.09)
	CG2	41.58(2.92)	45.71(2.51)	47.00(0.29)	43.25(2.21)	48.07(2.12)	45.59(0.25)
	CG2red	44.53(2.17)	45.18(3.18)	47.00(0.29)	46.21(2.77)	48.21(2.44)	45.59(0.250)
$\langle D_n \rangle$		near	overall	D_{melt}	near	overall	D_{melt}
	AA	0.96	0.83	0.063(0.003)	1.16	0.79	0.033(0.003)
	CG1	-	0.47	0.033(0.001)	-	0.54	0.020(0.001)
	CG1red	0.85	0.78	0.033(0.001)	1.11	0.98	0.020(0.001)
	CG2	-	0.41	0.017(0.001)	-	0.41	0.012(0.001)
CG2red	0.88	0.92	0.017(0.0010)	0.97	0.79	0.012(0.001)	

gion) from the differences in the composite system, allowing specific optimization of TPS and MMT cross-interactions. For the CG1 set, $\langle R_g \rangle$ and S_c ratios at $\gamma = 0.21$ and D_n at $\gamma = 0.25$ were closest to those in AA simulations, with $\langle R_g \rangle$ and S_c at $\gamma = 0.25$ and D_n at $\gamma = 0.21$ also in very good agreement with AA. A re-scaling factor of $\gamma = 0.21$ was found most suitable for self-interaction of MMT beads,⁸⁷ and therefore, the same factor was chosen here for the TPS-MMT cross-interactions for the CG1 parameter set (referred to as CG1red). For the CG2 parameter set, all three properties are in excellent agreement with AA at $\gamma = 0.15$ and represent a

distinct improvement over all other choices, and therefore, selected as CG2 parameter set for the composite system (referred to as CG2red).

The selected parameter set that concurrently optimize structural, thermodynamic, and dynamic properties are expected to provide an accurate estimate for other properties not used in optimization and also have better state-point transferability.^{77,109,110} For example, the addition of miscibility data in MARTINI-3 FF development¹⁰⁶ allowed for a significant improvement in some of the key limitations of MARTINI-2 FF concerning large self-interaction of some species (such as polysaccha-

rides) in solution,^{79,80} poor reproduction of liquid properties at interfaces.⁸²

3.3 TPS-MMT Composite Properties from the CG Model

Several properties of the composite system obtained using the different CG FFs were compared with the corresponding values obtained from AA simulations, and the inter-relationship between these properties was investigated. A single clay sheet sandwiched between two large TPS regions forms the model system S11, which provides the simplest setup for separate determination of properties in the near-sheet and far-sheet ("bulk") regions while also allowing for establishing a chemical equilibrium between these regions.

3.3.1 TPS Components' Density Profiles Above the TMA-MMT Sheet

The two plasticizers, water and sorbitol, show a sharp density peak near the TMA-MMT surface (Figure 5), driven by the interaction between their highly polar hydroxyl groups and TMA-MMT silicate layer with mobile ions. This preferential adsorption of water and sorbitol leads to depletion of polymer chains at the sheet surface, but polymer density shows a sharp increase within the first solvation layer,

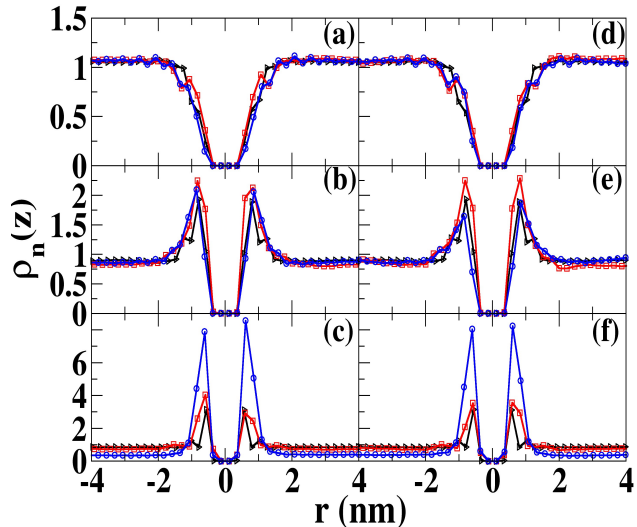


Figure 5: Density profile in TPS-MMT composite. Normalized density perpendicular to the TMA-MMT sheet (placed in xy plane), $\rho_n(z)$, for (a,d) polymer, (b,e) sorbitol, and (c,f) water. CG parameter set 1 is in (a-c) and set 2 in (d-f), with AA as \triangle , CG as \square , and CGred as \circ .

increasing to $\sim 50\%$ of the bulk value. This mixing of polymer and low molecular weight plasticizers in the interfacial region is possibly driven by the presence of polar beads, viz. diol (P4), hemiacetal (P1), and acetal (Na or P2), groups in the polymer chain. This provides one reason for an observed increase in TPS intercalation with increased water content in a TPS-clay (bentonite nanoclay) composite.¹⁹ Figure 5(a, d) shows that the scale of interactions (regular ($\gamma = 1$) or reduced) have essentially no effect on the normalized density of polymer beads. This directly follows from high polymer depletion at the sheet surface, which reduces the direct effect of TPS-TMA-MMT bead interactions. The choice of CG model (CG1 versus CG2) also has a negligible effect, partly because

of the density scaling by corresponding values in the melt system. Overall, all four CG models (CG1/2, regular/reduced) show an excellent agreement with CG and AA density profiles, $\rho_n(z)$, for polymer and sorbitol. However, there is a significant increase in water density at the clay surface (Figure 5(c, f)) for the CGred models. This implies that TPS-TMA-MMT cross-interactions are not fully optimized, with very low water content (1%) possibly accentuating the effect of sub-optimal interactions. All component densities reach a plateau (close to the bulk value) at an average z -distance of 2.5 nm from the TMA-MMT sheet, indicating minimal influence of the clay sheet beyond this distance. Therefore, the plane at $z = 2.5$ nm was used to distinguish between the near-clay and far regions for subsequent calculation of all reported properties.

3.3.2 Polymer Chain Conformation and Dynamics

Average chain conformation was characterized using radius of gyration, topological constraints and correlations using conformational entropy, and overall polymer dynamics using segment diffusion coefficients, all expected to show a significant dependence on polymer-surface interactions. In the AA simulations, the near-to-far $\langle R_g \rangle$ and S_c ratios, and amylose and

amylopectin trimeric segment D_n were close to unity. It is expected that favorable polymer-surface interactions lead to chain expansion, lower S_c , and lower D_n in the near-surface regions (w.r.t. bulk) while unfavorable interactions lead to the opposite effect. For example, AA simulations showed that strongly attractive polymer-surface interactions for polyethylene oxide-Na-MMT¹¹¹ lead to doubling of $\langle R_g \rangle$ and a decrease in diffusion coefficient in this system as well as in polyethylene-graphite composite.¹¹² Weakly attractive interactions for polyethylene, polypropylene, and polystyrene near the TMA-MMT sheet lead to a $\sim 10\%$ decrease in both S_c and diffusion coefficients.⁸⁷ Conversely, the addition of repulsive nanoparticles to a LJ polymer accelerated chain dynamics^{113,114} but had a negligible effect on $\langle R_g \rangle$.^{113,115} For the TPS-MMT system, the interplay of polymer-surface (weakly repulsive), plasticizer-surface (attractive), and polymer-plasticizer (weakly attractive) interactions lead to polymer depletion at the clay surface and a sharp increase in the density in the first solvation shell of plasticizers at the surface (Figure 5). This tempering of direct polymer-clay interactions and polymer-plasticizer mixing in the near clay region gave comparable $\langle R_g \rangle$, S_c , and D_n values in the near-clay and the far regions. In a similar ternary composite system of cellu-

lose nanocrystals (CNC)-polyvinylpyrrolidone (PVP)-polycaprolactone (PCL), PVP $\langle R_g \rangle$ increased from ~ 0.90 nm (unfavorable PVP-CNC interactions lowered $\langle R_g \rangle$ w.r.t. bulk) to 1.65 nm on addition of dichloromethane (DCM), a good solvent for PVP that pushed the PVP chains away from CNC.¹¹⁶ The use of standard TPS-MMT cross-interactions in CG1 and CG2 gave smaller near to far $\langle R_g \rangle$ and S_c ratios than AA: in the range 0.92-0.97 for $\langle R_g \rangle$ and 0.9-0.92 for S_c in CG compared to ~ 0.98 for both ratios in AA. The D_n in the composite was significantly lower ($\sim 0.4 - 0.5$) than that in AA ($\sim 0.8 - 0.9$) (Figure S9). As discussed in Section 3.2.3, the solid-fluid interactions are typically overestimated in MARTINI FF,^{82,98} leading to chain flattening and lower S_c and D_n . Therefore, TPS-MMT cross-interactions were rescaled as per Equation 5, which has built-in asymmetry leading to a smaller reduction in the pair interaction strength involving more polar beads. An excellent agreement with AA values was obtained for $\langle R_g \rangle$, S_c , and D_n at $\gamma = 0.21$ for CG1 (referred to as CG1red) and $\gamma = 0.15$ for CG2 (referred to as CG2red). The high level of rescaling is directly linked to the high covalent coordination state of the polymer chain and the MMT beads¹, shown to signifi-

¹A different value of re-scale parameter γ for cross-interactions involving non-ring sorbitol and water beads would have been more appropriate but potentially af-

cantly lower the dispersive interactions in earlier studies.^{87,91} This use of multiple properties in CG parameter optimization is expected to provide improved state-point transferability as shown in previous studies, for example, use of multiple state point optimization⁷⁷ or addition of density correction¹⁰⁹ in IBI-derived potentials, use of polymer hydration thermodynamics and structural properties in a CG FF combining MARTINI FF with IBI.¹¹⁰

3.3.3 Radial Distribution Function and Two-body Excess Entropy

Table 3: Normalized two-body excess entropy in TPS-TMA-MMT composite system. $S_{2,\alpha,\beta}$ were calculated from the average RDFs shown in Figure 6. The composite $S_{2,\alpha,\beta}$ values are reported after dividing with the respective $S_{2,\alpha,\beta}$ of TPS melt (Table S1). P and S refer to polymer (amylose and amylopectin) and sorbitol, respectively.

Pairs	near			far		
	P-P	P-S	S-S	P-P	P-S	S-S
AA	0.87	1.23	1.07	0.79	1.19	1.23
CG1	1.81	2.03	1.32	0.63	0.79	0.81
CG1red	1.69	1.05	0.83	0.60	0.79	0.81
CG2	2.00	2.60	1.16	0.60	0.91	0.86
CG2red	1.14	1.45	0.95	0.60	0.91	0.84

We have further evaluated CG1 and CG2 parameter sets by comparing estimates for radial distribution function and two-body excess entropy in the composite system to corresponding AA simulations, neither of which were used in parameter optimization. In the TPS-MMT

affected transferability and therefore, was not pursued

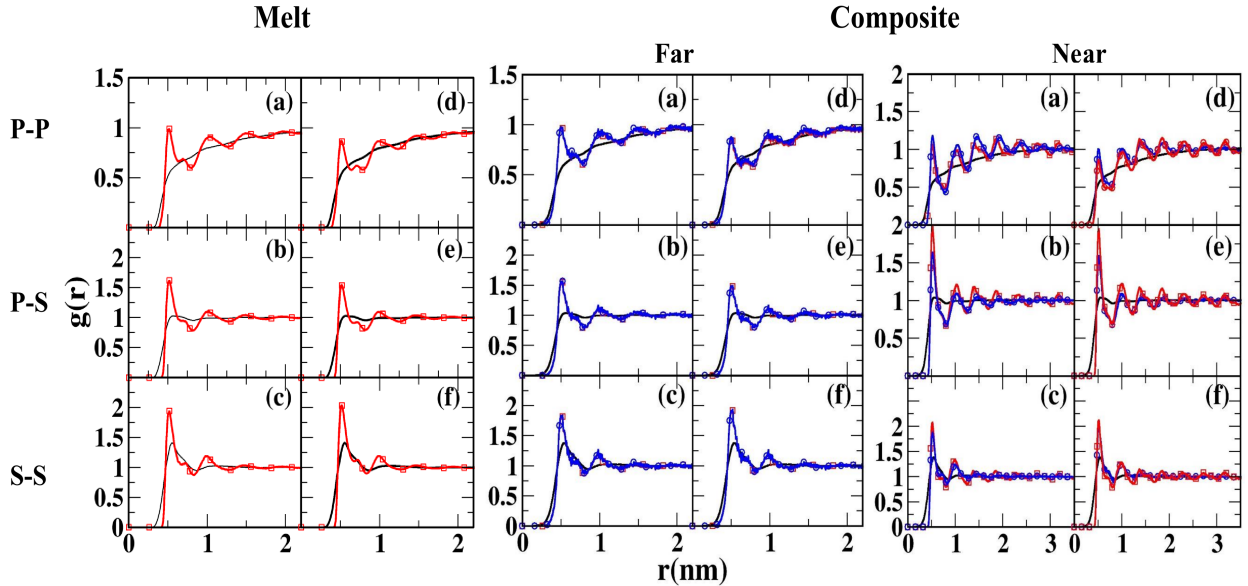


Figure 6: Radial distribution functions in TPS melt and TPS–MMT–TMA composite. RDFs for polymer-polymer (P-P), polymer-sorbitol (P-S), and sorbitol-sorbitol (S-S) beads in the melt and in near- and far-regions in the composite (2D RDF): **(a-c)** $g_{\alpha\beta}$ for AA (—), CG1 (— \square —), and CG1red (— \circ —), and **(d-f)** $g_{\alpha\beta}$ for AA (—), CG2 (— \square —), and CG2red (— \circ —). Four bonded atoms were excluded from all RDF calculations.

composite system, the polymer-polymer (PP), polymer-sorbitol (PS), and sorbitol-sorbitol (SS) 2D *RDFs* in the far region were identical to the melt (Figure 6), indicating a negligible effect of clay on the structural properties of TPS at a distance (along sheet normal) of $\sim 2\langle R_g \rangle$ from the sheet. The corresponding RDFs for CG1 and CG2 parameters are in good agreement, with the size of the first solvation shell and the order of first-peak heights (SS \lesssim PS \lesssim PP) the same as AA simulations. However, at the full level of TPS-MMT interaction (used in CG1 and CG2), the near-sheet *RDFs* show long-range structuring for all three pairs (Figure 6). A 1:1 comparison of AA and CG RDFs is not easy since the peaks show a broadening in AA RDFs because of the use of COM

of atoms making the CG bead. Therefore, individual pairwise ($S_{2,\alpha,\beta}$) and total two-body excess entropy (S_2), integrals over RDF calculated as per Equations ??, were used for a quantitative comparison between AA and CG simulations (Table S1). The near-region $S_{2,\alpha,\beta}$ values for CG1 and CG2 are up to 108% and 130% higher (in magnitude) than AA simulations, respectively. An increase in peak height and long-range structuring were directly linked to highly attractive liquid-solid surface interactions,¹¹³ a known drawback of MARTINI 2 forcefield as discussed for CG parameterization. The use of CG1red and CG2red parameter sets lead to both a lowering of first-peak height and a reduction in long-range structuring in near-region RDFs (Figure 6). The relative er-

rors (w.r.t AA) in near-region $S_{2,\alpha,\beta}$ calculated for CG1red simulations were 94%, 15%, and 22% for polymer-polymer, polymer-sorbitol, and sorbitol-sorbitol respectively (an improvement of 14%, 50%, and 1% over CG1), while for CG2red simulations were 31%, 18%, and 11% (an improvement of 99%, 93%, and -3% (this became slightly less accurate) over CG2), respectively. The success of the developed parameter set in accurately capturing diverse material properties beyond those used for optimization suggests their broad applicability for material characterization.

4 Conclusions

Enthalpy-based coarse-graining methods, such as DPD, require a state-dependent effective interaction parameter, wherein the phase space for its determination is significantly expanded for high system heterogeneity, for example, in the case of a TPS-MMT-TMA composite investigated in this work. Chemical-specific coarse-grained (CG) models, such as IBI, force-matching, or MARTINI, provide more effective parameterization for such systems. Here, we used AA simulation to predict several TPS properties, spanning from macroscopic (the glass transition temperature, Young’s modulus) to microscopic (conformation along 1-4

and 1-6 glycosidic linkages). These properties were used as constraints in developing an accurate MARTINI-2 FF parameter set for TPS melt. While existing MARTINI FF parameters obtained using the data from AA simulations of mono- and disaccharides in polar and apolar solvents⁸⁴ form a good starting point, several important differences between AA and CG simulations were observed for chain conformation and thermodynamic properties of a TPS melt. We used the data from AA simulations in the present work and bead-type assignments for similar functional groups used in literature^{79,80,84,107,108} to obtain a new parameter set for TPS melt, referred to as the CG2 parameter set. It included a shortening of the CG bond involving the 1-4 glycosidic link, an s-type bead for the hemiacetal group, Na bead type for the acetal group, one level reduction in the self-interaction of polymer diol bead, a small increase in the 1-4-7 angle from its value for amylose in apolar solvent, and a doubling of the force constants for 1-4-5 and 1-4-6 angles. The CG2 model provided simultaneous improvement in several structural and thermodynamic properties of TPS melt, making it a distinct improvement over existing MARTINI FF parameters for TPS.

The AA simulation of the TPS-MMT system revealed that the interplay of polymer-surface

(weakly repulsive), plasticizer-surface (attractive), and polymer-plasticizer (weakly attractive) interactions lead to preferential adsorption of the plasticizer and depletion of polymer at the clay surface, and mixing of polymer and plasticizer within the first solvation shell, a feature captured very well by the optimized CG models used in this study. This unique density profile also resulted in comparable R_g , S_c , and D_n in near-clay and far regions, making it distinct from the expected behavior for attractive or repulsive polymer-surface interactions in simpler systems. However, the CG simulation of the TPS-MMT composite showed compaction and flattening of polymer chains (lower R_g) and significantly reduced dynamics (lower S_c and D_n) in the near-sheet region. The use of liquid-liquid partition coefficients in MARTINI-2 parameterization makes it inherently less suitable for solid-liquid interfaces, with an unphysical freezing of liquid at a solid interface reported in several previous studies. In the present case, a high covalent coordination state for the polymer chains and MMT sheet, shown to significantly lower the dispersive interactions, further accentuated this effect. The downscaling of the effective dispersive component of the TPS-MMT MARTINI-2 interaction parameter led to simultaneous improvement in R_g , S_c , and D_n , with the selected

CG2red parameter set giving D_n for amylose within 10 % of AA and all other values (for both amylose and amylopectin) within 5 %. CG1red and CG2red models also significantly improved over the corresponding full interaction models (CG1 and CG2) in predicting two-body excess entropy (calculated from the radial distribution function). Thus, the developed MARTINI-2 CG parameters for TPS-MMT composites, which offer close to a hundred-fold speedup over AA simulations, can be used to accurately estimate properties not used in parameterization.

We acknowledge that rescaling the sheet-TPS interaction is a sub-optimal solution that potentially limits transferability to systems with very different components. The optimal bead type assignments determined in this study, combined with a significant expansion of bead types and availability of scale factors for cross- and self-interaction in the recently released MARTINI-3 FF can allow for more rational development of parameters for various TPS-clay composites.

Acknowledgement The authors thank the IIT Delhi High-Performance Computing (HPC) facility for providing the computational resources.

References

- (1) Carvalho, A. J. Starch: major sources, properties and applications as thermoplastic materials. *Monomers, polymers and composites from renewable resources* **2008**, 321–342.
- (2) Jiménez, A.; Fabra, M.; Talens, P.; Chiralt, A. Edible and biodegradable starch films: a review. *Food Bioprocess Technol* **5** (6): 2058–2076. 2012.
- (3) Attaran, S. A.; Hassan, A.; Wahit, M. U. Materials for food packaging applications based on bio-based polymer nanocomposites: A review. *Journal of Thermoplastic Composite Materials* **2017**, *30*, 143–173.
- (4) Babu, R. P.; O’connor, K.; Seeram, R. Current progress on bio-based polymers and their future trends. *Progress in biomaterials* **2013**, *2*, 1–16.
- (5) Khan, B.; Bilal Khan Niazi, M.; Samin, G.; Jahan, Z. Thermoplastic starch: A possible biodegradable food packaging material—A review. *Journal of Food Process Engineering* **2017**, *40*, e12447.
- (6) Stepto, R. The processing of starch as a thermoplastic. *Macromolecular Symposia*. 2003; pp 203–212.
- (7) de Freitas, A. d. S. M.; da Silva, A. P. B.; Montagna, L. S.; Nogueira, I. A.; Carvalho, N. K.; de Faria, V. S.; Dos Santos, N. B.; Lemes, A. P. Thermoplastic starch nanocomposites: sources, production and applications—a review. *Journal of Biomaterials Science, Polymer Edition* **2022**, *33*, 900–945.
- (8) Kaboorani, A.; Gray, N.; Hamzeh, Y.; Abdulkhani, A.; Shirmohammadli, Y. Tailoring the low-density polyethylene-thermoplastic starch composites using cellulose nanocrystals and compatibilizer. *Polymer Testing* **2021**, *93*, 107007.
- (9) Corrêa, A. C.; de Campos, A.; Claro, P. I. C.; Guimarães, G. G. F.; Mattoso, L. H. C.; Marconcini, J. M. Biodegradability and nutrients release of thermoplastic starch and poly (ϵ -caprolactone) blends for agricultural uses. *Carbohydrate Polymers* **2022**, *282*, 119058.
- (10) Cyras, V. P.; Manfredi, L. B. Physical and mechanical properties of thermoplastic starch / montmorillonite nanocomposite films. **2008**, *73*, 55–63.
- (11) Chocyk, D.; Gladyszewska, B.; Ciupak, A.; Oniszczyk, T.; Moscicki, L.; Rejak, A. Influence of water addition on mechanical properties of thermoplastic starch foils. *International Agrophysics*

- 2015**, *29*.
- (12) Domene-López, D.; García-Quesada, J. C.; Martín-Gullon, I.; Montalbán, M. G. Influence of starch composition and molecular weight on physicochemical properties of biodegradable films. *Polymers* **2019**, *11*, 1084.
- (13) Salaberria, A. M.; Diaz, R. H.; Labidi, J.; Fernandes, S. C. Role of chitin nanocrystals and nanofibers on physical, mechanical and functional properties in thermoplastic starch films. *Food Hydrocolloids* **2015**, *46*, 93–102.
- (14) Rezaei, M.; Ismail, A. F.; Bakeri, G.; Hashemifard, S. A.; Matsuura, T. Effect of general montmorillonite and Cloisite 15A on structural parameters and performance of mixed matrix membranes contactor for CO₂ absorption. *Chemical Engineering Journal* **2015**, *260*, 875–885.
- (15) Zhou, M.; Xu, D. Starch-MMT composite films: Effects of bio-inspired modification on MMT. *Starch-Stärke* **2015**, *67*, 470–477.
- (16) Suter, J. L.; Groen, D.; Coveney, P. V. Chemically specific multiscale modeling of clay-polymer nanocomposites reveals intercalation dynamics, tactoid self-assembly and emergent materials properties. *Advanced Materials* **2015**, *27*, 966–984.
- (17) Altayan, M. M.; Al Darouich, T. Toward reducing the food packaging waste impact: a study on the effect of Starch type and PE type in thermoplastic starch-polyethylene blends. *Chemical Papers* **2022**, *76*, 2447–2457.
- (18) Baumberger, S.; Lapierre, C.; Monties, B.; Della Valle, G. Use of kraft lignin as filler for starch films. *Polymer Degradation and Stability* **1998**, *59*, 273–277.
- (19) Park, H.-M.; Li, X.; Jin, C.-Z.; Park, C.-Y.; Cho, W.-J.; Ha, C.-S. Preparation and properties of biodegradable thermoplastic starch/clay hybrids. *Macromolecular Materials and Engineering* **2002**, *287*, 553–558.
- (20) Schlemmer, D.; Angélica, R. S.; Sales, M. J. A. Morphological and thermomechanical characterization of thermoplastic starch/montmorillonite nanocomposites. *Composite Structures* **2010**, *92*, 2066–2070.
- (21) Majdzadeh-Ardakani, K.; Navarchian, A. H.; Sadeghi, F. Optimization of mechanical properties of thermoplastic starch/clay nanocomposites. *Carbohydrate Polymers* **2010**, *79*, 547–554.
- (22) Rivadeneira-Velasco, K. E.; Utreras-

- Silva, C. A.; Díaz-Barrios, A.; Sommer-Márquez, A. E.; Tafur, J. P.; Michell, R. M. Green nanocomposites based on thermoplastic starch: A review. *Polymers* **2021**, *13*, 3227.
- (23) Huang, M. F.; Yu, J. G.; Ma, X. F. Studies on the properties of Montmorillonite-reinforced thermoplastic starch composites. *Polymer* **2004**, *45*, 7017–7023.
- (24) Krishnamoorti, R.; Vaia, R. A.; Gianelis, E. P. Structure and dynamics of polymer-layered silicate nanocomposites. *Chemistry of Materials* **1996**, *8*, 1728–1734.
- (25) Alias, A. H.; Norizan, M. N.; Sabaruddin, F. A.; Asyraf, M. R. M.; Norrahim, M. N. F.; Ilyas, A. R.; Kuzmin, A. M.; Rayung, M.; Shazleen, S. S.; Nazrin, A.; others Hybridization of MMT/lignocellulosic fiber reinforced polymer nanocomposites for structural applications: a review. *Coatings* **2021**, *11*, 1355.
- (26) Ayana, B.; Suin, S.; Khatua, B. Highly exfoliated eco-friendly thermoplastic starch (TPS)/poly (lactic acid)(PLA)/clay nanocomposites using unmodified nanoclay. *Carbohydrate polymers* **2014**, *110*, 430–439.
- (27) Mao, C.; Zhu, Y.; Jiang, W. Design of electrical conductive composites: Tuning the morphology to improve the electrical properties of graphene filled immiscible polymer blends. *ACS Applied Materials and Interfaces* **2012**, *4*, 5281–5286.
- (28) Huang, F.; Zhou, S. Molecular Dynamics Simulation of Coiled Carbon Nanotube Pull-Out from Matrix. *International Journal of Molecular Sciences* **2022**, *23*, 9254.
- (29) Guo, L.; Xu, H.; Wu, N.; Yuan, S.; Zhou, L.; Wang, D.; Wang, L. Molecular dynamics simulation of the effect of the thermal and mechanical properties of addition liquid silicone rubber modified by carbon nanotubes with different radii. *e-Polymers* **2023**, *23*, 20228105.
- (30) Lin, K.; Wang, Z. Multiscale mechanics and molecular dynamics simulations of the durability of fiber-reinforced polymer composites. *Communications Materials* **2023**, *4*, 66.
- (31) Gartner III, T. E.; Jayaraman, A. Modeling and simulations of polymers: a roadmap. *Macromolecules* **2019**, *52*, 755–786.
- (32) Guvench, O.; Greene, S. N.; Kamath, G.; Brady, J. W.; Venable, R. M.; Pastor, R. W.; Mackerell Jr, A. D. Additive empirical force field for hexopyra-

- nose monosaccharides. *Journal of computational chemistry* **2008**, *29*, 2543–2564.
- (33) Hatcher, E.; Guvench, O.; MacKerell Jr, A. D. CHARMM additive all-atom force field for aldopentofuranoses, methyl-aldopentofuranosides, and fructofuranose. *The Journal of Physical Chemistry B* **2009**, *113*, 12466–12476.
- (34) Geronimo, I.; Ntarima, P.; Piens, K.; Gudmundsson, M.; Hansson, H.; Sandgren, M.; Payne, C. M. Kinetic and molecular dynamics study of inhibition and transglycosylation in *Hypocrea jecorina* family 3 β -glucosidases. *Journal of Biological Chemistry* **2019**, *294*, 3169–3180.
- (35) Kirschner, K. N.; Yongye, A. B.; Tschampel, S. M.; González-Outeiriño, J.; Daniels, C. R.; Foley, B. L.; Woods, R. J. GLYCAM06: a generalizable biomolecular force field. Carbohydrates. *Journal of computational chemistry* **2008**, *29*, 622–655.
- (36) Plazinski, W.; Lonardi, A.; Hünenberger, P. H. Revision of the GROMOS 56A6CARBO force field: improving the description of ring-conformational equilibria in hexopyranose-based carbohydrates chains. *Journal of computational chemistry* **2016**, *37*, 354–365.
- (37) Özeren, H. D.; Olsson, R. T.; Nilsson, F.; Hedenqvist, M. S. Prediction of plasticization in a real biopolymer system (starch) using molecular dynamics simulations. *Materials & Design* **2020**, *187*, 108387.
- (38) Özeren, H. D.; Guivier, M.; Olsson, R. T.; Nilsson, F.; Hedenqvist, M. S. Ranking Plasticizers for Polymers with Atomistic Simulations: PVT, Mechanical Properties, and the Role of Hydrogen Bonding in Thermoplastic Starch. *ACS Applied Polymer Materials* **2020**, *2*, 2016–2026.
- (39) Koneru, J. K.; Zhu, X.; Mondal, J. Quantitative Assessment of the Conformational Heterogeneity in Amylose across Force Fields. *Journal of Chemical Theory and Computation* **2019**, *15*, 6203–6212.
- (40) Mazeau, K.; Heux, L. Molecular dynamics simulations of bulk native crystalline and amorphous structures of cellulose. *The Journal of Physical Chemistry B* **2003**, *107*, 2394–2403.
- (41) Gatsiou, C. A.; Bick, A.; Krokidis, X.; Economou, I. G. Atomistic and Coarse-Grained Simulations of Bulk Amorphous Amylose Above and Below the Glass Transition. *Macromolecules* **2022**,

- (42) Groot, R. D.; Warren, P. B. Dissipative particle dynamics: Bridging the gap between atomistic and mesoscopic simulation. *Journal of Chemical Physics* **1997**, *107*, 4423–4435.
- (43) Singh, A.; Chakraborti, A.; Singh, A. Role of a polymeric component in the phase separation of ternary fluid mixtures: A dissipative particle dynamics study. *Soft Matter* **2018**, *14*, 4317–4326.
- (44) Fu, Y.; Liao, L.; Yang, L.; Lan, Y.; Mei, L.; Liu, Y.; Hu, S. Molecular dynamics and dissipative particle dynamics simulations for prediction of miscibility in polyethylene terephthalate/polylactide blends. *Molecular Simulation* **2013**, *39*, 415–422.
- (45) Scocchi, G.; Posocco, P.; Fermeglia, M.; Pricl, S. Polymer - Clay nanocomposites: A multiscale molecular modeling approach. *Journal of Physical Chemistry B* **2007**, *111*, 2143–2151.
- (46) Long, D.; Sotta, P. Nonlinear and plastic behavior of soft thermoplastic and filled elastomers studied by dissipative particle dynamics. *Macromolecules* **2006**, *39*, 6282–6297.
- (47) Sliozberg, Y. R.; Gair Jr, J. L.; Hsieh, A. J. Dissipative particle dynamics simulation of microphase separation in polyurethane urea nanocomposites. *Polymer* **2020**, *193*, 122339.
- (48) Khani, S.; Jamali, S.; Boromand, A.; Hore, M. J.; Maia, J. Polymer-mediated nanorod self-assembly predicted by dissipative particle dynamics simulations. *Soft Matter* **2015**, *11*, 6881–6892.
- (49) Wang, J.; Han, Y.; Xu, Z.; Yang, X.; Ramakrishna, S.; Liu, Y. Dissipative particle dynamics simulation: A review on investigating mesoscale properties of polymer systems. *Macromolecular Materials and Engineering* **2021**, *306*, 2000724.
- (50) Ju, S.-P.; Wang, Y.-C.; Huang, G.-J.; Chang, J.-W. Miscibility of graphene and poly (methyl methacrylate)(PMMA): molecular dynamics and dissipative particle dynamics simulations. *Rsc Advances* **2013**, *3*, 8298–8307.
- (51) Schweizer, K. S.; Honnell, K. G.; Curro, J. G. Reference interaction site model theory of polymeric liquids: Self-consistent formulation and nonideality effects in dense solutions and melts. *The Journal of chemical physics* **1992**, *96*, 3211–3225.
- (52) Schweizer, K. S.; Fuchs, M.; Szamel, G.; Guenza, M.; Tang, H. Polymer-mode-coupling theory of the slow dynamics of entangled macromolecular fluids. *Macro-*

- molecular theory and simulations* **1997**, *6*, 1037–1117.
- (53) Zirkel, A.; Gruner, S.; Urban, V.; Thiagarajan, P. Small-angle neutron scattering investigation of the Q-dependence of the Flory- Huggins interaction parameter in a binary polymer blend. *Macromolecules* **2002**, *35*, 7375–7386.
- (54) Wu, J. Density functional theory for chemical engineering: From capillarity to soft materials. *AIChE journal* **2006**, *52*, 1169–1193.
- (55) Oxtoby, D. W. Density functional methods in the statistical mechanics of materials. *Annual Review of Materials Research* **2002**, *32*, 39.
- (56) Helfand, E.; Sapse, A. M. Theory of unsymmetric polymer–polymer interfaces. *The Journal of chemical physics* **1975**, *62*, 1327–1331.
- (57) Helfand, E.; Wasserman, Z. R. Block copolymer theory. 4. Narrow interphase approximation. *Macromolecules* **1976**, *9*, 879–888.
- (58) Lowden, L. J.; Chandler, D. Solution of a new integral equation for pair correlation functions in molecular liquids. *The Journal of Chemical Physics* **1973**, *59*, 6587–6595.
- (59) Sung, B. J.; Yethiraj, A. Integral equation theory of randomly coupled multi-block copolymer melts: Effect of block size on the phase behavior. *The Journal of chemical physics* **2005**, *123*, 214901.
- (60) Hall, L. M.; Schweizer, K. S. Impact of monomer sequence, composition and chemical heterogeneity on copolymer-mediated effective interactions between nanoparticles in melts. *Macromolecules* **2011**, *44*, 3149–3160.
- (61) Martin, T. B.; Jayaraman, A. Using theory and simulations to calculate effective interactions in polymer nanocomposites with polymer-grafted nanoparticles. *Macromolecules* **2016**, *49*, 9684–9692.
- (62) Hsu, C.; Chandler, D. RISM calculation of the structure of liquid chloroform. *Molecular Physics* **1979**, *37*, 299–301.
- (63) Martin, T. B.; Gartner III, T. E.; Jones, R. L.; Snyder, C. R.; Jayaraman, A. pyPRISM: a computational tool for liquid-state theory calculations of macromolecular materials. *Macromolecules* **2018**, *51*, 2906–2922.
- (64) Clark, A. J.; Guenza, M. G. Mapping of polymer melts onto liquids of soft-colloidal chains. **2010**, 1–13.
- (65) Clark, A. J.; Mccarty, J.; Lyubimov, I. Y.; Guenza, M. G. Thermodynamic Consistency in Variable-Level

- Coarse Graining of Polymeric Liquids. **2012**, *168301*, 1–5.
- (66) Lyubimov, I. Y.; Mccarty, J.; Clark, A.; Guenza, M. G. Analytical rescaling of polymer dynamics from mesoscale simulations. **2010**, 1–6.
- (67) Lyubimov, I. Y.; Guenza, M. G. Theoretical reconstruction of realistic dynamics of highly coarse-grained cis-1,4-polybutadiene melts Theoretical reconstruction of realistic dynamics of highly coarse-grained. **2013**, *546*.
- (68) McCarty, J.; Guenza, M. G. Multiscale modeling of binary polymer mixtures: Scale bridging in the athermal and thermal regime. *Journal of Chemical Physics* **2010**, *133*.
- (69) Karatrantos, A.; Clarke, N.; Kröger, M. Modeling of polymer structure and conformations in polymer nanocomposites from atomistic to mesoscale: A Review. *Polymer reviews* **2016**, *56*, 385–428.
- (70) Zeng, Q.; Yu, A.; Lu, G. Multiscale modeling and simulation of polymer nanocomposites. *Progress in polymer science* **2008**, *33*, 191–269.
- (71) Gooneie, A.; Schuschnigg, S.; Holzer, C. A review of multiscale computational methods in polymeric materials. *Polymers* **2017**, *9*, 16.
- (72) Glotzer, S. C.; Paul, W. Molecular and mesoscale simulation methods for polymer materials. *Annual Review of materials research* **2002**, *32*, 401–436.
- (73) Reith, D.; Meyer, H.; Müller-Plathe, F. Mapping atomistic to coarse-grained polymer models using automatic simplex optimization to fit structural properties. *Macromolecules* **2001**, *34*, 2335–2345.
- (74) Reith, D.; Pütz, M.; Müller-Plathe, F. Deriving effective mesoscale potentials from atomistic simulations. *Journal of computational chemistry* **2003**, *24*, 1624–1636.
- (75) Izvekov, S.; Voth, G. A. A multiscale coarse-graining method for biomolecular systems. *The Journal of Physical Chemistry B* **2005**, *109*, 2469–2473.
- (76) Marrink, S. J.; Risselada, H. J.; Yefimov, S.; Tieleman, D. P.; De Vries, A. H. The MARTINI force field: Coarse grained model for biomolecular simulations. *Journal of Physical Chemistry B* **2007**, *111*, 7812–7824.
- (77) Moore, T. C.; Iacovella, C. R.; McCabe, C. Derivation of coarse-grained potentials via multistate iterative Boltzmann inversion. *The Journal of chemical physics* **2014**, *140*.
- (78) Panizon, E.; Boicchio, D.; Monti-

- celli, L.; Rossi, G. MARTINI coarse-grained models of polyethylene and polypropylene. *The Journal of Physical Chemistry B* **2015**, *119*, 8209–8216.
- (79) Schmalhorst, P. S.; Deluweit, F.; Scherers, R.; Heisenberg, C. P.; Sikora, M. Overcoming the Limitations of the MARTINI Force Field in Simulations of Polysaccharides. *Journal of Chemical Theory and Computation* **2017**, *13*, 5039–5053.
- (80) Shivgan, A. T.; Marzinek, J. K.; Huber, R. G.; Krah, A.; Henchman, R. H.; Matsudaira, P.; Verma, C. S.; Bond, P. J. Extending the Martini coarse-grained force field to N-Glycans. *Journal of Chemical Information and Modeling* **2020**, *60*, 3864–3883.
- (81) Wu, D.; Yang, X. Coarse-grained molecular simulation of self-assembly for non-ionic surfactants on graphene nanostructures. *The Journal of Physical Chemistry B* **2012**, *116*, 12048–12056.
- (82) Gobbo, C.; Beurroies, I.; de Ridder, D.; Eelkema, R.; Marrink, S. J.; De Feyter, S.; van Esch, J. H.; de Vries, A. H. MARTINI model for physisorption of organic molecules on graphite. *The Journal of Physical Chemistry C* **2013**, *117*, 15623–15631.
- (83) Piskorz, T. K.; Gobbo, C.; Marrink, S. J.; De Feyter, S.; De Vries, A. H.; Van Esch, J. H. Nucleation mechanisms of self-assembled physisorbed monolayers on graphite. *The Journal of Physical Chemistry C* **2019**, *123*, 17510–17520.
- (84) López, C. A.; Rzepiela, A. J.; de Vries, A. H.; Dijkhuizen, L.; Hünenberger, P. H.; Marrink, S. J. Martini coarse-grained force field: Extension to carbohydrates. *Journal of Chemical Theory and Computation* **2009**, *5*, 3195–3210.
- (85) Sukenik, S.; Sapir, L.; Harries, D. Osmolyte induced changes in peptide conformational ensemble correlate with slower amyloid aggregation: a coarse-grained simulation study. *Journal of Chemical Theory and Computation* **2015**, *11*, 5918–5928.
- (86) Michalowsky, J.; Schäfer, L. V.; Holm, C.; Smiatek, J. A refined polarizable water model for the coarse-grained MARTINI force field with long-range electrostatic interactions. *The Journal of Chemical Physics* **2017**, *146*, 054501.
- (87) Khan, P.; Goel, G. Martini Coarse-Grained Model for Clay-Polymer Nanocomposites. *Journal of Physical Chemistry B* **2019**, *123*, 9011–9023.

- (88) Guvench, O.; Hatcher, E.; Venable, R. M.; Pastor, R. W.; Mackerell Jr, A. D. CHARMM additive all-atom force field for glycosidic linkages between hexopyranoses. *Journal of chemical theory and computation* **2009**, *5*, 2353–2370.
- (89) Guvench, O.; Mallajosyula, S.; Raman, E.; Hatcher, E.; Vanommeslaeghe, K.; Foster, T.; Jamison, F. II and Mackerell AD Jr (2011) CHARMM additive all-atom force field for carbohydrate derivatives and its utility in polysaccharide and carbohydrate-protein modeling. *J Chem Theory Comput* *7*, 3162–3180.
- (90) Jo, S.; Kim, T.; Iyer, V. G.; Im, W. CHARMM-GUI: a web-based graphical user interface for CHARMM. *Journal of computational chemistry* **2008**, *29*, 1859–1865.
- (91) Heinz, H.; Koerner, H.; Anderson, K. L.; Vaia, R. A.; Farmer, B. Force field for mica-type silicates and dynamics of octadecylammonium chains grafted to montmorillonite. *Chemistry of materials* **2005**, *17*, 5658–5669.
- (92) Martínez, L.; Andrade, R.; Birgin, E. G.; Martínez, J. M. PACKMOL: a package for building initial configurations for molecular dynamics simulations. *Journal of computational chemistry* **2009**, *30*, 2157–2164.
- (93) Lyckfeldt, O.; Ferreira, J. M. Processing of Porous Ceramics by 'Starch Consolidation'. *Journal of the European Ceramic Society* **1998**, *18*, 131–140.
- (94) Abraham, M. J.; Murtola, T.; Schulz, R.; Páll, S.; Smith, J. C.; Hess, B.; Lindahl, E. GROMACS: High performance molecular simulations through multi-level parallelism from laptops to supercomputers. *SoftwareX* **2015**, *1*, 19–25.
- (95) Bussi, G.; Donadio, D.; Parrinello, M. Canonical sampling through velocity rescaling. *The Journal of chemical physics* **2007**, *126*.
- (96) Berendsen, H. J.; Postma, J. v.; Van Gunsteren, W. F.; DiNola, A.; Haak, J. R. Molecular dynamics with coupling to an external bath. *The Journal of chemical physics* **1984**, *81*, 3684–3690.
- (97) Parrinello, M.; Rahman, A. Polymorphic transitions in single crystals: A new molecular dynamics method. *Journal of Applied physics* **1981**, *52*, 7182–7190.
- (98) Yesylevskyy, S. O.; Schäfer, L. V.; Sengupta, D.; Marrink, S. J. Polarizable water model for the coarse-grained MARTINI force field. *PLoS computational bi-*

- ology* **2010**, *6*, e1000810.
- (99) Williams, M. L.; Landel, R. F.; Ferry, J. D. The temperature dependence of relaxation mechanisms in amorphous polymers and other glass-forming liquids. *Journal of the American Chemical Society* **1955**, *77*, 3701–3707.
- (100) Sharma, R.; Agarwal, M.; Chakravarty, C. Estimating the entropy of liquids from atom–atom radial distribution functions: Silica, beryllium fluoride and water. *Molecular Physics* **2008**, *106*, 1925–1938.
- (101) Schlitter, J. Estimation of absolute and relative entropies of macromolecules using the covariance matrix. *Chemical physics letters* **1993**, *215*, 617–621.
- (102) Gessler, K.; Usón, I.; Takaha, T.; Krauss, N.; Smith, S. M.; Okada, S.; Sheldrick, G. M.; Saenger, W. V-amylose at atomic resolution: X-ray structure of a cycloamylose with 26 glucose residues (cyclomaltohexaicosaoase). *Proceedings of the National Academy of Sciences of the United States of America* **1999**, *96*, 4246–4251.
- (103) Patel, D. S.; Pendrill, R.; Mallajosyula, S. S.; Widmalm, G.; MacKerell, A. D. Conformational properties of α - Or β -(1→6)-linked oligosaccharides: Hamiltonian replica exchange MD simulations and NMR experiments. *Journal of Physical Chemistry B* **2014**, *118*, 2851–2871.
- (104) Forssell, P. M.; Mikkilä, J. M.; Moates, G. K.; Parker, R. Phase and glass transition behaviour of concentrated barley starch-glycerol-water mixtures, a model for thermoplastic starch. *Carbohydrate Polymers* **1997**, *34*, 275–282.
- (105) Zartman, G. D.; Liu, H.; Akdim, B.; Pachter, R.; Heinz, H. Nanoscale tensile, shear, and failure properties of layered silicates as a function of cation density and stress. *The Journal of Physical Chemistry C* **2010**, *114*, 1763–1772.
- (106) Souza, P. C.; Alessandri, R.; Barnoud, J.; Thallmair, S.; Faustino, I.; Grünewald, F.; Patmanidis, I.; Abdizadeh, H.; Bruininks, B. M.; Wassenaar, T. A.; others Martini 3: a general purpose force field for coarse-grained molecular dynamics. *Nature methods* **2021**, *18*, 382–388.
- (107) Hsu, P.-C.; Jefferies, D.; Khalid, S. Molecular dynamics simulations predict the pathways via which pristine fullerenes penetrate bacterial membranes. *The journal of physical chemistry*

- B* **2016**, *120*, 11170–11179.
- (108) Wohler, J.; Berglund, L. A. A coarse-grained model for molecular dynamics simulations of native cellulose. *Journal of Chemical Theory and Computation* **2011**, *7*, 753–760.
- (109) Hu, C.; Lu, T.; Guo, H. Developing a transferable coarse-grained model for the prediction of thermodynamic, structural, and mechanical properties of polyimides at different thermodynamic state points. *Journal of chemical information and modeling* **2019**, *59*, 2009–2025.
- (110) Banerjee, P.; Roy, S.; Nair, N. Coarse-grained molecular dynamics force-field for polyacrylamide in infinite dilution derived from iterative Boltzmann inversion and MARTINI force-field. *The Journal of Physical Chemistry B* **2018**, *122*, 1516–1524.
- (111) Suter, J. L.; Coveney, P. V. Computer simulation study of the materials properties of intercalated and exfoliated poly(ethylene) glycol clay nanocomposites. *Soft Matter* **2009**, *5*, 2239–2251.
- (112) Daoulas, K. C.; Harmandaris, V. A.; Mavrantzas, V. G. Detailed atomistic simulation of a polymer melt/solid interface: structure, density, and conformation of a thin film of polyethylene melt adsorbed on graphite. *Macromolecules* **2005**, *38*, 5780–5795.
- (113) Smith, G. D.; Bedrov, D.; Li, L.; Bytner, O. A molecular dynamics simulation study of the viscoelastic properties of polymer nanocomposites. *The Journal of chemical physics* **2002**, *117*, 9478–9489.
- (114) Varnik, F.; Baschnagel, J.; Binder, K. Reduction of the glass transition temperature in polymer films: A molecular-dynamics study. *Physical Review E* **2002**, *65*, 021507.
- (115) Karatrantos, A.; Clarke, N.; Composto, R. J.; Winey, K. I. Polymer conformations in polymer nanocomposites containing spherical nanoparticles. *Soft Matter* **2015**, *11*, 382–388.
- (116) Voronova, M. I.; Gurina, D. L.; Surov, O. V.; Zakharov, A. G. Interactions in solvent–polycaprolactone–cellulose nanocrystals–polyvinyl pyrrolidone system: Experiment and molecular dynamics simulation. *Journal of Molecular Liquids* **2021**, *341*, 117409.

5 Supplementary Material

5.1 Temperature-pressure annealing cycles

The initial box, obtained using Packmol software, underwent a multi-step density increase followed by multiple temperature-pressure (T-P) cycles to obtain an equilibrated TPS structure free from the memory effect of the initial configuration. The coordinates of the simulation box were rescaled in steps of 29.17 nm³ followed by energy minimization at each step using the steepest decent algorithm. The T-P annealing cycles were performed on the rescaled TPS system (state A) to accelerate the slow dynamics of the starch chains, leading to a more rapid attainment of the equilibrated configuration. (Figure S1). The simulation time at the lower (613K) and higher temperature (613K) of the annealing cycle was chosen to ensure local equilibration (potential energy plateau) and Brownian relaxation of the chain, respectively (Figure S1 (A)). Following the completion of each temperature cycle, the pressure was incrementally doubled. Once a pressure of 1000 bar was reached, the system was depressurized back to 1 bar using the same stepwise approach (Figure S1 (C)). The complete T-P cycles were repeated until the density of the initial (state A) and final (state A') states matched (Figure S1 (C)).

5.2 Key Results

Table S1: Two-body excess entropy of TPS melt system The two-body excess entropies for polymer-sorbitol pairs were calculated by integrating the RDF (Figure 6) of the corresponding pairs in the TPS melt, using Equation 3.

System	TPS melt		
pairs	Polymer-Polymer	Polymer-Sorbitol	Sorbitol-Sorbitol
AA	-1.33	-0.36	-0.52
CGLITa	-1.29	-0.75	-0.57
CGLITb	-1.39	-0.67	-0.61
CGSSa-S	-0.95	-0.40	-0.95
CG1	-1.21	-0.58	-0.83
CG2	-1.30	-0.44	-0.98

The $S_{2,\alpha\beta}$ of polymer-sorbitol pair were calculated using Equation S1

$$S_{2,\alpha\beta} = -\pi\rho \int_0^\infty g_{\alpha\beta}(r) \ln g_{\alpha\beta}(r) - [g_{\alpha\beta}(r) - 1] r dr \tag{S1}$$

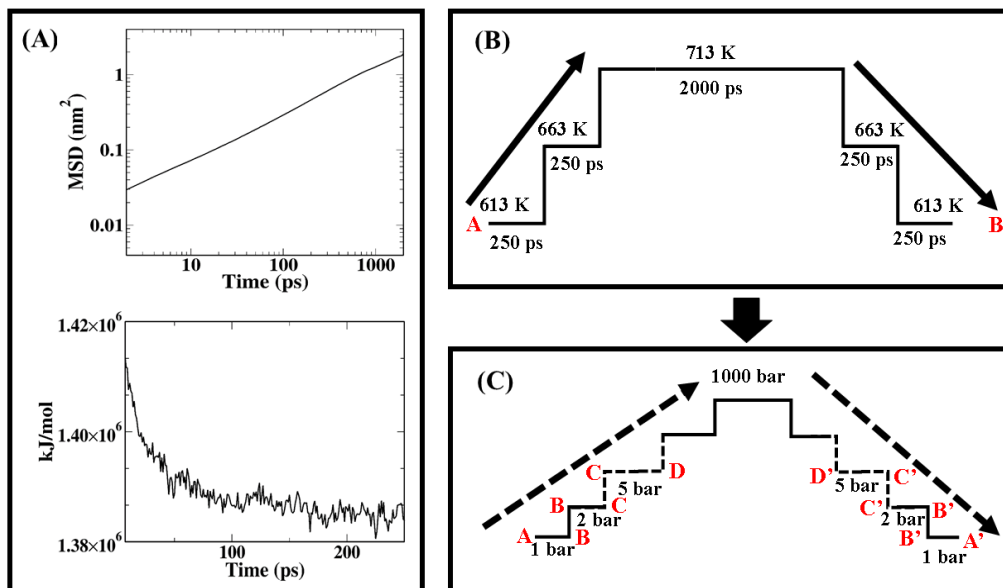


Figure S1: Temperature-pressure annealing simulations **A** The MSD (at 713 K) and potential energy plateau (at 613 K), used to estimate simulation time and temperature in annealing cycle required in temperature annealing cycles (shown in **B**) to attain Brownian relaxation time and local equilibration of TPS melt, respectively. **B** In the temperature annealing cycle, states A and B represent the rescaled input and output simulation boxes, respectively. **C** T-P annealing cycle workflow along with the pressure values.

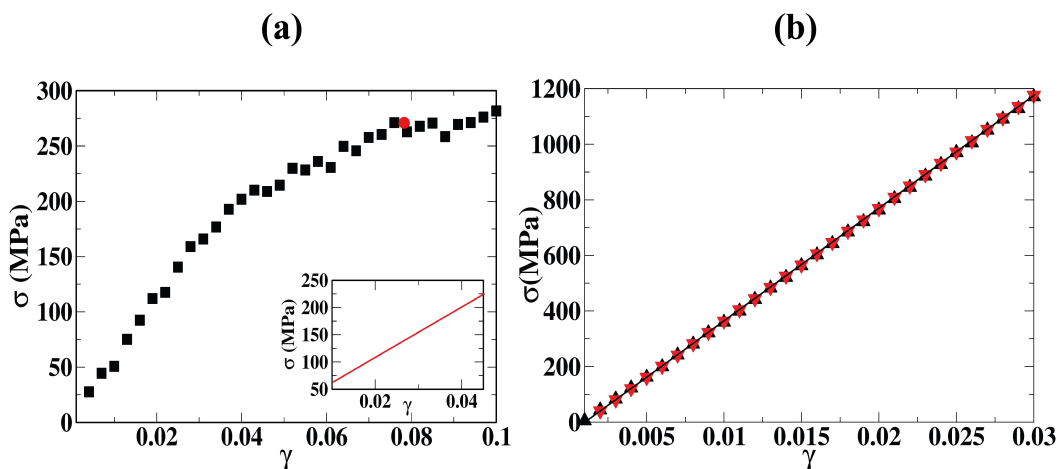


Figure S2: Stress-strain behavior of the TPS melt and MMT sheet **(a)** The linear part of TPS stress-strain data (represented by ---) was used to estimate Young's modulus. The onset of the plateau (maximum stress) is represented by \bullet . **(b)** The AA (\blacktriangle) and CG (\blacktriangledown) stress data of the TMA-MMT sheet. The system was stretched using a series of 0.1% unidirectional (in the x -direction) strains (at 300 K, and 1 bar) and the corresponding Virial (P_{xx}) values at each step were used to estimate the stress.

The diffusion coefficients were calculated using the Equation S2.

$$MSD(t) = 6 \cdot D \cdot t \quad (S2)$$

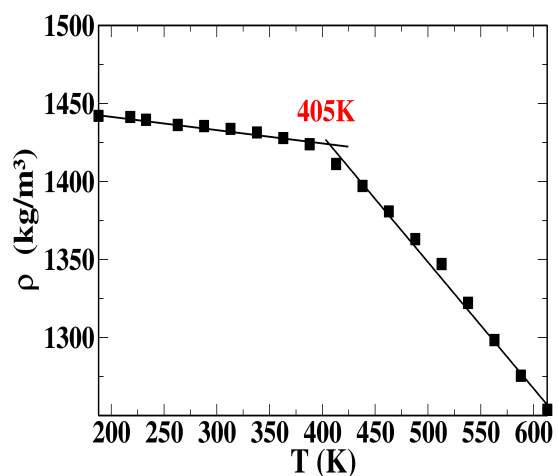


Figure S3: Density-temperature plot for TPS melt The TPS melt system was cooled from 613 K to 150 K in steps of 25 K, where 4 ns NPT simulation was performed at each step, with last 500 ps trajectory at each step used for density calculation. The intersection point (highlighted in red) of rubbery and glassy region lines is used as an estimate of glass-transition temperature.

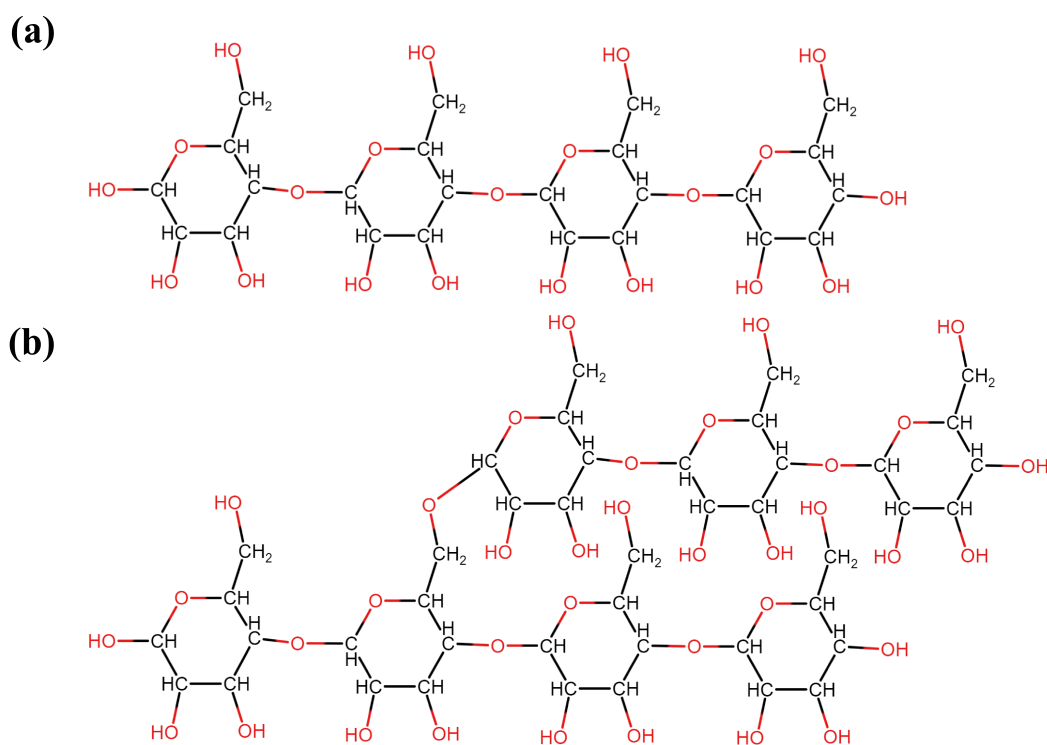


Figure S4: Chemical structure of amylose and amylopectin . A chemical representation of (a) amylose and (b) amylopectin chain consisting of four and seven α -D glucose monomers, respectively.

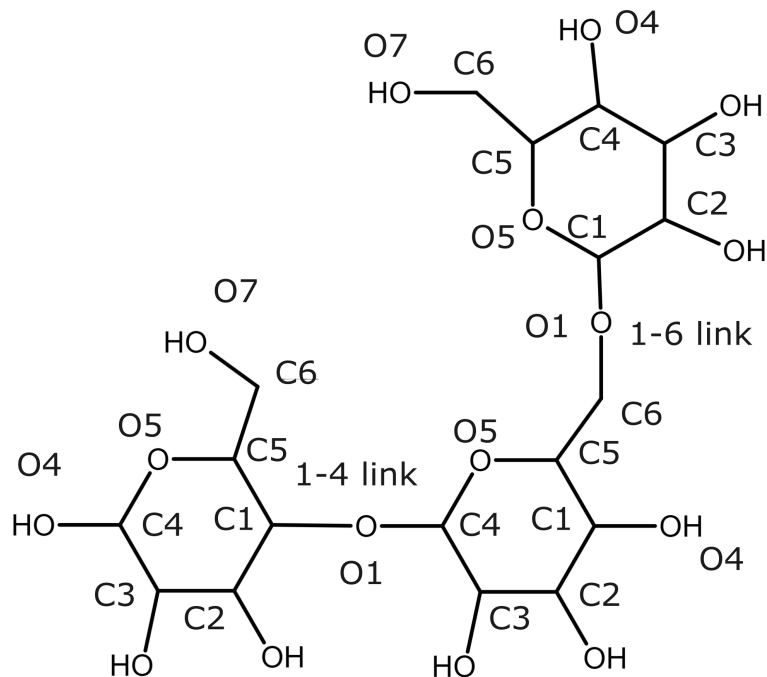


Figure S5: AA representation of 1-4 and 1-6 linkage . The 1-4 α -D glucose linkage is represented by $\phi = \angle O_5 - C_4 - O_1 - C_1$, $\psi = \angle C_1 - O_1 - C_4 - C_3$, and 1-6 α -D glucose linkage is represented by $\phi = \angle O_5 - C_1 - O_1 - C_6$, $\psi = \angle C_1 - O_1 - C_6 - C_5$.

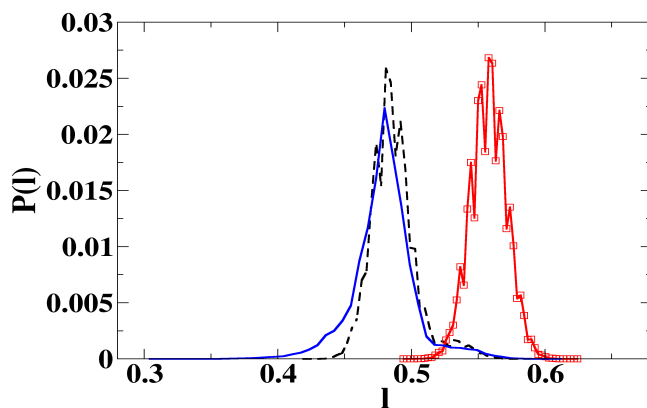


Figure S6: AA and CG angle distribution of amylopectin y-axis show the probability distribution ($P(l)$) of 1-4 glycosidic bond (l) for AA(---), CG1(- \square -), and CG2(—) models. The distribution obtained from TPS melt simulation at 613K and 1 bar

5.3 CG-MARTINI parameters

The center of mass positions of functional groups (corresponding to CG beads) in AA trajectories were converted to pseudo-CG trajectories using Equation S3.

$$r_i^{\text{CG}} = \frac{\sum_{j=1}^n r_j m_j}{\sum_{j=1}^n m_j} \quad (\text{S3})$$

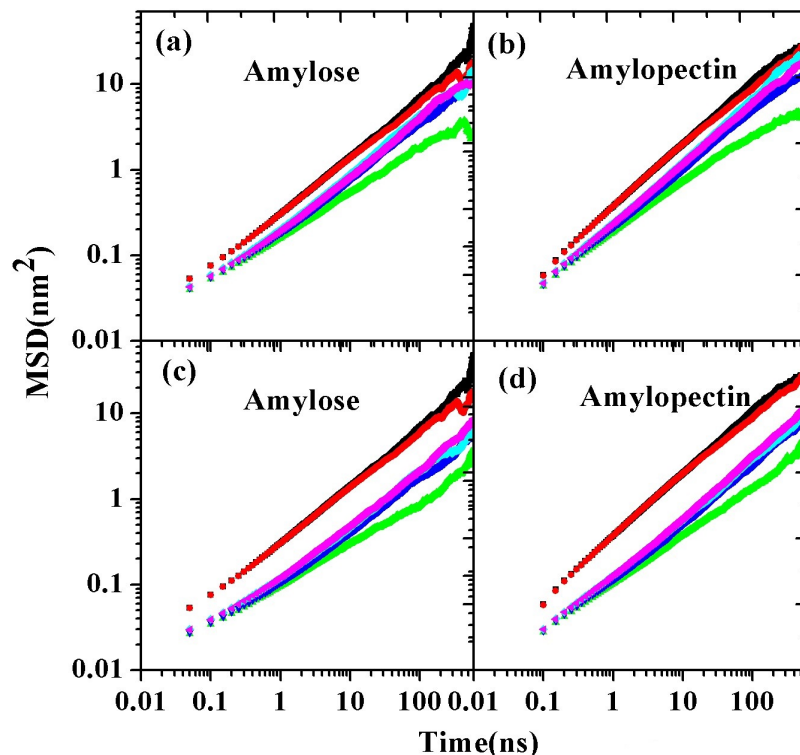


Figure S7: MSD for TPS-MMT composite system The MSD of amylose and amylopectin trimeric segments were estimated for CG1 (a,b) and CG2 (c,d) models. MSDs in Near-MMT regions for AA (■), CG (▲), and CGred (▼) and far-MMT regions for AA (●), CG (▼), and CGred (◆) are estimated from TPS-TMA-MMT simulation at 613 K and 1 bar

Where, m_j and r_i are the masses and positions of atoms, r_i^{CG} are the positions for pseudo-CG beads.

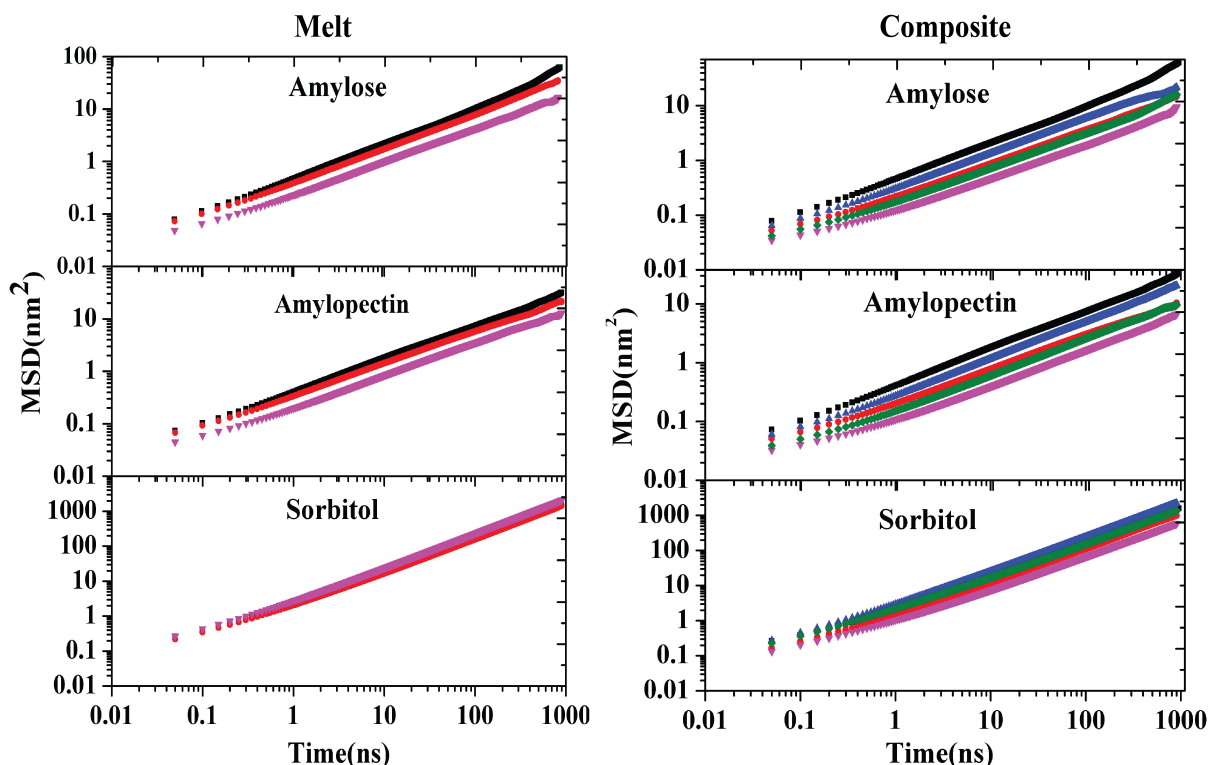


Figure S8: MSD of TPS components in melt and composite systems MSD for AA (■), CG1 (●), CG1red (▲), CG2 (▼), and CG2red (◆) were estimated at 613K and 1 bar. In the composite system, the MSD was calculated in the x - y plane using an equilibrated trajectory of 900 ns

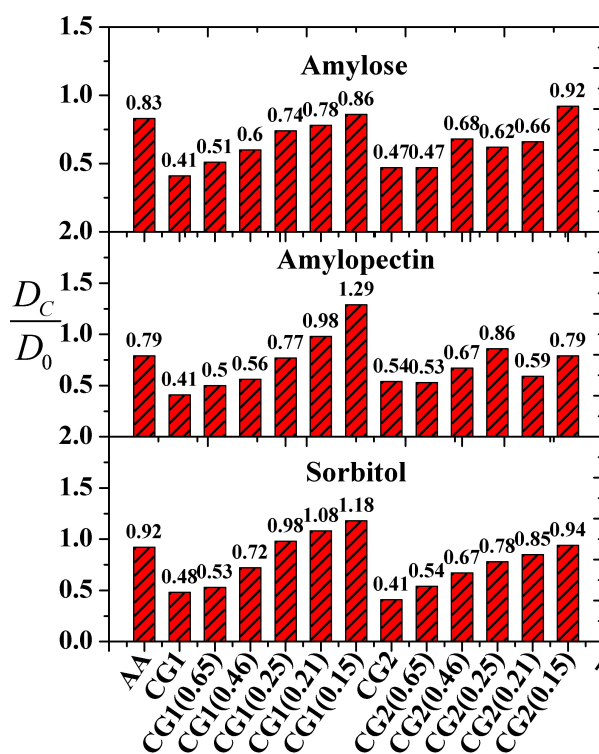


Figure S9: Normalized diffusion coefficient of TPS components The diffusion coefficients of TPS components in melt (D_0) and composite (D_c) were obtained from the slope of MSD (shown in Figure S8) in the linear regime. The $MSDs$ were calculated from 900 ns long simulation trajectories, obtained at a temperature of 613K and a pressure of 1 bar

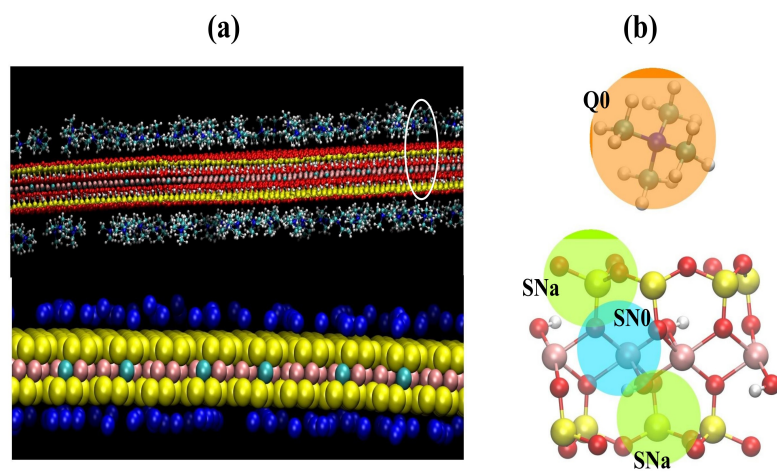
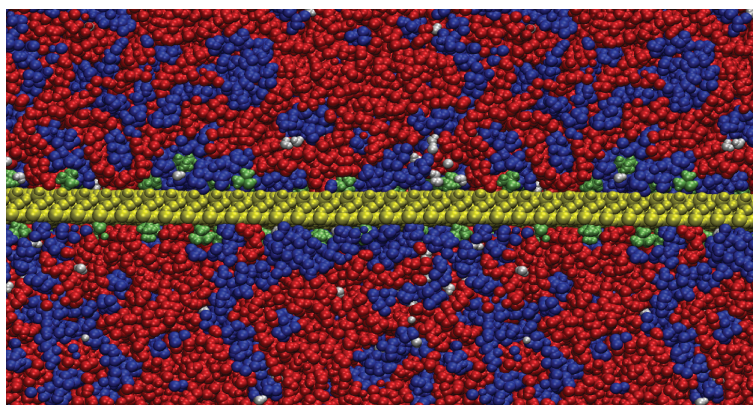
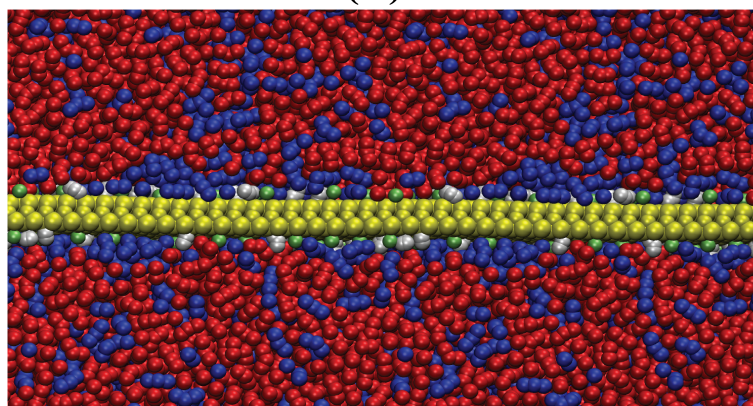


Figure S10: AA and CG representation of TMA-MMT sheet with the Mapping scheme. (a) shows the AA and CG representation of the TMA-MMT sheet. (b) shows the mapping scheme and MARTINI bead type of the highlighted portion of the sheet in (a)



(A)



(B)

Figure S11: AA and CG representation of TPS-TMA-MMT composite system. (a) shows the AA representation of the composite system. (b) shows the same system in CG representation. The red, blue, yellow, and lime colors represent the polymer, sorbitol, water, and MMT, respectively.

Table S2: CG MARTINI bonded parameter 1-4 and 1-6 glycosidic links The bonded parameter obtained from the AA simulation of TPS melt system at 613K and 1 bar. The columns show force constants k_l , k_θ , and k_ϕ of bonds (l_0), angles (θ), and dihedrals (ϕ_0), respectively. Figure 1 illustrates the nomenclature used to represent beads.

type	topological pattern	parameters			
bonds		l_0	k_l [kJ mol ⁻¹ nm ⁻⁴]	function	
	1-2	0.238	30000	1	
	1-3	0.276	30000	1	
	4-5	0.224	30000	1	
	4-6	0.244	30000	1	
1-4 link	1-4	0.482	30000	1	
1-6 link	1-6	0.300	30000	1	
angle		θ_0	k_θ [kJ mol ⁻¹]	function	
	2-1-4	70	100	2	
	3-1-4	50	25	2	
	1-4-5	140	100	2	
	1-4-6	140	100	2	
1-4 link	1-4-7	125	180	2	
1-6 link	4-6-1	100	55	2	
	6-1-2	140	45	2	
	6-1-3	140	35	2	
dihedrals		ϕ_0	k_ϕ [kJ mol ⁻¹]	function	multiplicity
	2-1-4-5	120	8	1	1
	2-1-4-6	-20	5	1	1
	3-1-4-5	-40	5	1	1
1-6 link	4-6-1-2	-100	5	1	1

Table S3: MARTINI non-bonded parameter of TPS melt. The listed bead diameter (σ_{ij}) and interaction strength (ϵ_{ij}) were used in stimulating the TPS melt system (for both the CG1 and CG2 models). The bead assignments are shown in Figure 1. The P4c bead is a variant of P4 that employs a weaker level II self-interaction compared to level I in P4

Bead type		σ (nm)	ϵ (kJ mol ⁻¹)
P4c	P4c	0.47	4.500
P4c	Na	0.47	4.000
P4c	SP1	0.47	4.500
POL	SP1	0.47	3.800
POL	Na	0.47	3.325
POL	P4c	0.47	4.275
POL	POL	0.47	3.100

Table S4: MARTINI non-bonded parameter of TPS-TMA–MMT composite system. The Table illustrates the bead diameter (σ_{ij}) and the rescaled interaction strengths (ϵ_{ij}) between TPS and MMT beads ($\gamma=0.15$). The SN0, SQ0, and SNa are MMT sheet beads representing AlO_2H , MgO_2H , and SiO_2 , respectively.

	Bead type	σ (nm)	ϵ (kJ mol^{-1})
SN0	P1	0.47	1.025
SN0	P2	0.47	1.025
SN0	P4c	0.47	1.025
SN0	Na	0.47	0.525
SN0	SP1	0.43	0.769
SNa	P1	0.47	1.525
SNa	P2	0.47	1.525
SNa	P4c	0.47	1.525
SNa	Na	0.47	1.025
SNa	SP1	0.43	1.144
SQ0	P1	0.47	1.025
SQ0	P2	0.47	1.525
SQ0	P4c	0.47	2.625
SQ0	Na	0.47	1.025
SQ0	SP1	0.43	0.769
SQ0	SQ0	0.43	0.560
SNa	SNa	0.43	0.935
SN0	SN0	0.43	0.560

Table S5: Comparison of AA and CG properties of TPS-MMT composite system The radius of gyration ($\langle R_g \rangle$) and configuration entropy per CG bead (S_c) were calculated for six different resealing factors (γ) in range of 0.15 to 1. All properties calculated at 613 K and 1 bar.

		Amylose			Amylopectin			
		γ	near	far	melt	near	far	melt
$\langle R_g \rangle$ (nm)	AA		1.35	1.37	1.38	1.74	1.77	1.83
	CG1	1	1.49	1.57	1.58	1.95	2.01	2.07
		0.65	1.47	1.58	1.58	2.00	2.05	2.07
		0.44	1.51	1.58	1.58	2.01	2.03	2.07
		0.25	1.52	1.58	1.58	1.97	2.01	2.07
		0.21	1.53	1.56	1.58	1.99	1.99	2.07
		0.15	1.52	1.59	1.58	2.03	2.09	2.07
	CG2	1	1.34	1.45	1.43	1.78	1.84	1.83
		0.65	1.39	1.47	1.43	1.76	1.82	1.83
		0.44	1.37	1.43	1.43	1.77	1.83	1.83
		0.25	1.37	1.41	1.43	1.79	1.85	1.83
		0.21	1.40	1.43	1.43	1.78	1.83	1.83
		0.15	1.38	1.40	1.43	1.78	1.84	1.83
	$\langle S_c \rangle$ (J mol ⁻¹ K)	AA		46.11	46.73	46.26	45.82	46.63
CG1		1	44.44	48.68	52.16	47.09	51.41	51.90
		0.65	45.95	49.02	52.16	47.07	51.66	51.90
		0.44	44.81	48.74	52.16	48.71	51.93	51.90
		0.25	47.64	48.65	52.16	49.68	51.61	51.90
		0.21	48.23	48.31	52.16	50.30	51.58	51.90
		0.15	48.31	48.54	52.16	50.72	51.99	51.90
CG2		1	41.58	45.71	47.00	43.25	48.07	45.59
		0.65	41.97	46.23	47.00	41.76	48.45	45.59
		0.44	41.27	47.03	47.00	43.35	49.23	45.59
		0.25	43.38	45.96	47.00	45.09	48.12	45.59
		0.21	43.19	45.96	47.00	45.79	48.22	45.59
		0.15	44.53	45.19	47.00	46.21	48.21	45.59

TOC Graphic

